Detection and characterization of 0.5–8 MeV neutrons near Mercury: Evidence for a solar origin

David J. Lawrence,[1] William C. Feldman,[2] John O. Goldsten,[1] Patrick N. Peplowski,[1] Douglas J. Rodgers,[1] and Sean C. Solomon[3,4]

Received 16 May 2013; revised 19 September 2013; accepted 8 February 2014; published 9 July 2014.

[1] Data from the MErcury Surface, Space ENvironment, GEochemistry, and Ranging (MESSENGER) Neutron Spectrometer (NS) have been used to identify energetic neutrons (0.5–8 MeV energy) associated with solar events that occurred on 4 June 2011. Multiple lines of evidence, including measurements from the NS and the MESSENGER Gamma-Ray Spectrometer, indicate that the detected neutrons have a solar origin. This evidence includes a lack of time-coincident, energetic (>45 MeV) charged particles that could otherwise create local neutrons from nearby spacecraft material and a lack of proton-induced gamma rays that should be seen if energetic protons were present. NS data cannot rule out the presence of lower-energy ions (<30 MeV) that can produce local neutrons. However, the ion spectral shape required to produce the measured neutron count rate locally is softer than any known ion spectral shape. The neutron energy spectrum shows a relative enhancement in the energy range 0.8–3 MeV compared with cosmic-ray-generated neutrons from the spacecraft or Mercury. The spectral shape of the measured neutron fluence spectrum is consistent with a previously modeled fluence spectrum of neutrons that originate at the Sun and are propagated through the MESSENGER spacecraft to the NS. These measurements provide strong evidence for a solar origin of the detected neutrons and suggest that a large number of low-energy threshold ion evaporation reactions were taking place on the Sun during the neutron event.

Citation: Lawrence, D. J., W. C. Feldman, J. O. Goldsten, P. N. Peplowski, D. J. Rodgers, and S. C. Solomon (2014), Detection and characterization of 0.5–8 MeV neutrons near Mercury: Evidence for a solar origin, *J. Geophys. Res. Space Physics*, *119*, 5150–5171, doi:10.1002/2013JA019037.

1. Introduction

[2] Solar neutrons are produced through interactions between energetic ions and the solar atmosphere. Because neutrons are not affected by the Sun's magnetic field, they can readily escape from the Sun and provide direct information about energetic ions near the Sun, including the total flux of the ion population and how these ions are accelerated. *Dorman* [2010] and *Vilmer et al.* [2011] recently reviewed the history of solar neutron measurements and the information that can be gained from them. Solar neutrons are difficult to detect at Earth because they have a 15 min mean life, and all but the highest-energy (>100 MeV) neutrons decay prior to reaching 1 AU [*Ryan*, 2000]. Although low-energy neutrons (1–10 MeV) are virtually impossible to detect at Earth, they can provide key information about acceleration processes [*Hua et al.*, 2002; *Vilmer et al.*, 2011]. Specifically, low-energy solar neutrons can provide constraints on the rates of nuclear reactions between energetic ions and solar atmospheric ions with energy thresholds on the order of 1 MeV/nucleon as well as information on the ion acceleration spectrum in the range 1–100 MeV/nucleon [*Vilmer et al.*, 2001]. Because some energetic heavy ions have reaction thresholds below 1 MeV/nucleon for producing neutrons, low-energy solar neutrons can also provide constraints on the heavy-ion population near the Sun [*Vilmer et al.*, 2011].

[3] To detect 1–10 MeV neutrons with reasonable sensitivity, the distance of the neutron detector to the Sun must be substantially less than 1 AU. Measuring neutron spectra at a small detector-Sun distance was the rationale for considering the inclusion of neutron detectors on planned missions to the inner heliosphere (e.g., Solar Orbiter and Solar Probe Plus) [*Feldman et al.*, 1989; *Woolf et al.*, 2009; *Lawrence et al.*, 2014]. Unfortunately, neutron detectors were not selected for either of these missions. The only neutron detector currently operating within the inner heliosphere is the Neutron Spectrometer (NS) on the MErcury Surface, Space ENvironment, GEochemistry, and Ranging (MESSENGER) spacecraft. The NS was designed to measure the surface

[1]The Johns Hopkins University Applied Physics Laboratory, Laurel, Maryland, USA.
[2]Planetary Science Institute, Tucson, Arizona, USA.
[3]Department of Terrestrial Magnetism, Carnegie Institution of Washington, Washington, District of Columbia, USA.
[4]Lamont-Doherty Earth Observatory, Columbia University, Palisades, New York, USA.

Corresponding author: D. J. Lawrence, The Johns Hopkins University Applied Physics Laboratory, Laurel, Maryland, USA. (David.J.Lawrence@jhuapl.edu)

2169-9380/14/10.1002/2013JA019037

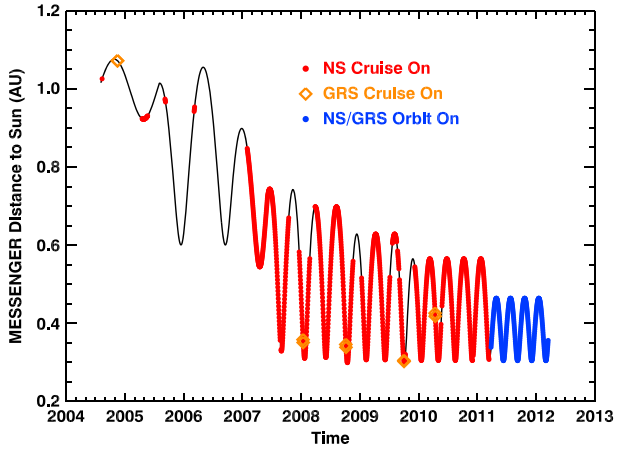

Figure 1. Summary of MESSENGER's distance from the Sun between launch on 3 August 2004 and the end of the primary mission in March 2012. NS and GRS operations are shown in colored symbols (NS cruise operation shown by red circles, GRS cruise operation shown by orange squares, and NS/GRS orbital operation by blue circles).

composition of Mercury with planetary neutron spectroscopy [*Goldsten et al.*, 2007]. Specifically, the NS measures neutrons in the energy range between less than 1 eV and ~8 MeV. Fast neutrons ($0.5 < E_n < 8$ MeV, where E_n is the neutron energy) are measured using a coincidence pulse processing technique whereby the initial neutron energy is measured via proton recoil reactions in a BC454 plastic scintillator and the slowed-down neutron is identified via a $^{10}B(n,\alpha)$ capture reaction in the scintillator. *Feldman et al.* [2010] provided additional details of the fast-neutron detection capability of the NS. The MESSENGER spacecraft was launched in August 2004 and was inserted into orbit about Mercury in March 2011. During the 6.6 year heliocentric cruise phase, the aphelion distance of the MESSENGER spacecraft from the Sun was gradually reduced to 0.42 AU (Figure 1). Early in the interplanetary cruise phase of the MESSENGER mission, the NS was periodically turned on for health and safety checks. Since early 2007, the NS has been operating in a near-continuous manner. Figure 1 shows a summary of the NS operation from launch to the present.

[4] Although NS data are used primarily for studies of Mercury's surface composition [e.g., *Lawrence et al.*, 2010, 2013], MESSENGER's location at 0.3–0.4 AU provides opportunities for making measurements of solar phenomena. From MESSENGER NS data, *Feldman et al.* [2010] reported the first detection of low-energy (1–8 MeV) solar neutrons from a large solar event on 31 December 2007. On the basis of the extended duration of the detected neutrons (up to 9 h), and because neutrons decay into protons and electrons with a mean time scale of less than 15 min, *Feldman et al.* [2010] suggested that the presence of such neutrons near the Sun would form an extended seed population of protons available for further acceleration by subsequent shocks driven by coronal mass ejections into interplanetary space.

[5] *Share et al.* [2011] questioned the solar origin of the neutrons detected from the 31 December 2007 event. Specifically, *Share et al.* [2011] suggested that the neutrons were locally produced at the spacecraft from energetic ions. *Feldman et al.* [2010] anticipated that concern and estimated that the maximum possible level of local neutron generation from charged particles was a factor of 5 lower than the detected level. In reply, *Share et al.* [2011] suggested that appropriate neutron production cross sections were not used for the *Feldman et al.* [2010] analysis; *Share et al.* [2011] provided alternative cross sections for calculating the local spacecraft production of neutrons.

[6] Here we report a new detection of fast neutrons likely of solar origin on 4 June 2011. The detection occurred 6 h prior to a large solar particle event that occurred on 4–5 June 2011. Unlike the 31 December 2007 event, no energetic charged-particle enhancement (>45 MeV protons) was observed during this later fast-neutron event. Therefore, this event has less ambiguity regarding the production location of the neutrons that may be present for the 31 December 2007 event. In addition, the MESSENGER Gamma-Ray Spectrometer (GRS), a high-purity Ge gamma ray detector, was operating in June 2011 but had not been powered on in December 2007. As we will argue, the GRS data, along with charged-particle data from the NS, provide critical information in support of a solar origin of the detected fast neutrons.

2. Solar Particle Event of 4–5 June 2011

[7] On 4 June 2011, a pair of flares with accompanying coronal mass ejections (CMEs) erupted from the Sun within direct view of the MESSENGER spacecraft. *Lario et al.* [2013] reported on the magnetic field and energetic electron intensities at MESSENGER associated with these flares. Figure 2 shows an image of the Sun at 195 nm wavelength obtained with the Extreme Ultraviolet Imager (EUVI) on the Solar TErrestrial RElations Observatory (STEREO) A spacecraft, with a red arrow indicating the solar disk location of the event, identified as NOAA Active Region 11224 [*Lario et al.*, 2013]. According to *Lario et al.* [2013], two successive CMEs were released from

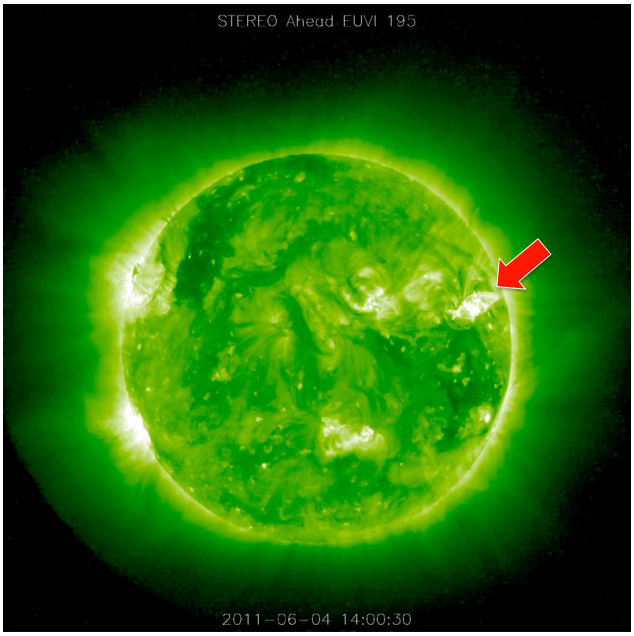

Figure 2. Image of the solar disk at 195 nm wavelength from STEREO-A/EUVI data taken on 4 June 2011 at 14:00:30 UTC. The location of the 4–5 June 2011 event is indicated by the red arrow.

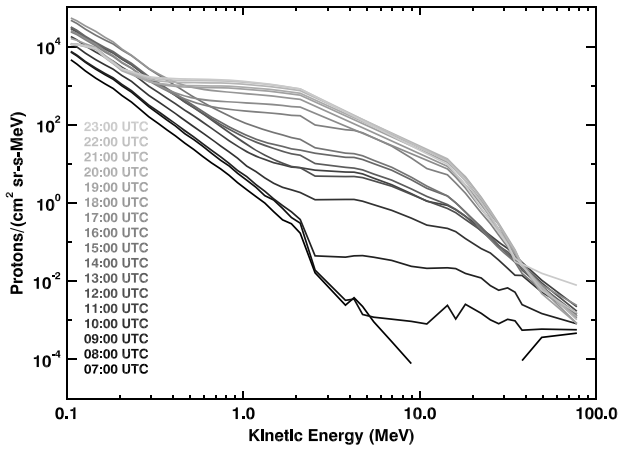

Figure 3. Proton fluxes measured at 1 AU from the STEREO-A SEPT, LET, and HET instruments. Energy spectra are shown for different hour-long durations from 07:00 to 23:00 UTC on 4 June 2011; indicated times are at the start of the intervals.

the identified active region, and the release times of these CMEs —06:45 and 21:45 UTC—were separated by approximately 15 h. A large flux of energetic particles hit MESSENGER on 4 June at 22:00 UTC [*Lario et al.*, 2013] (section 4). The presence of this large enhancement of energetic particles at 22:00 UTC was interpreted by *Lario et al.* [2013] as resulting from particle confinement between the two CME-driven shocks. A substantial enhancement of energetic particles was observed at STEREO-A as illustrated by proton fluxes (Figure 3) from the Solar Electron Proton Telescope (SEPT), Low Energy Telescope (LET), and High Energy Telescope (HET).

3. MESSENGER NS Fast-Neutron Data on 4–5 June 2011

[8] MESSENGER fast-neutron data measured between late 3 June 2011 and early 5 June 2011 are shown in Figure 4a. During that time, the MESSENGER spacecraft was in a 12 h eccentric orbit around Mercury with a periapsis of a few hundred kilometers and an apoapsis of around 15,000 km. The MESSENGER spacecraft altitude above Mercury's surface during this same time is shown in Figure 4b. For this study, we used the nominal NS fast-neutron detection threshold of 0.5 MeV. When the MESSENGER spacecraft is within 6000 km of Mercury's surface, the NS collects data with a 20 s cadence; at higher altitudes, the data collection cadence is 300 s.

[9] A number of points are illustrated by the data in Figure 4. First, on 4 June 2011 there were two periapsis passes of Mercury at which the fast-neutron count rate rose from a background value of <2 counts per second (cps) to >10 cps. This count rate enhancement is the nominal flux of fast neutrons coming from the surface of Mercury as induced by energetic galactic cosmic rays (GCRs) [e.g., *Maurice et al.*, 2000; *Lawrence et al.*, 2013]. The time variability of the fast neutrons is a function of Mercury's solid angle subtended by the field of view of the omnidirectional NS. When the MESSENGER spacecraft was farther than a few Mercury radii from the planet (Mercury's radius is 2440 km), the fast-neutron count rate returned to its nominal background level (e.g., between 2:00 and 10:00 UTC).

[10] At 15:45 UTC, there was a clear enhancement of fast neutrons that lasted for approximately 1 h. Since the MESSENGER spacecraft was far from Mercury at that time, these neutrons cannot have originated from Mercury. Figure 5 shows NS event mode data taken during 4 June 2011. NS event mode data are used for diagnostic purposes to provide an unambiguous identification of fast neutrons. Specifically, Figure 5a shows a histogram of the time to second pulse (TTSP) for three different time periods: during background periods when the altitude was $>10{,}000$ km, during Mercury periapsis passes when the altitude was <1500 km, and during the 15:45 to 16:45 UTC neutron enhancement. The TTSP histogram measures the elapsed time between the two pulses used to identify fast neutrons. The characteristic shape of the TTSP histogram in the BC454 plastic scintillator is an exponential count rate decrease for early times and a flat distribution for late times. For the BC454 scintillator, the exponential portion of the distribution has a ~2 μs characteristic decay, which indicates the mean time for an energy-moderated neutron to be captured by a ^{10}B atom in the scintillator. The histograms for all three time periods show the characteristic 2 μs decay, which indicates a positive detection of fast neutrons,

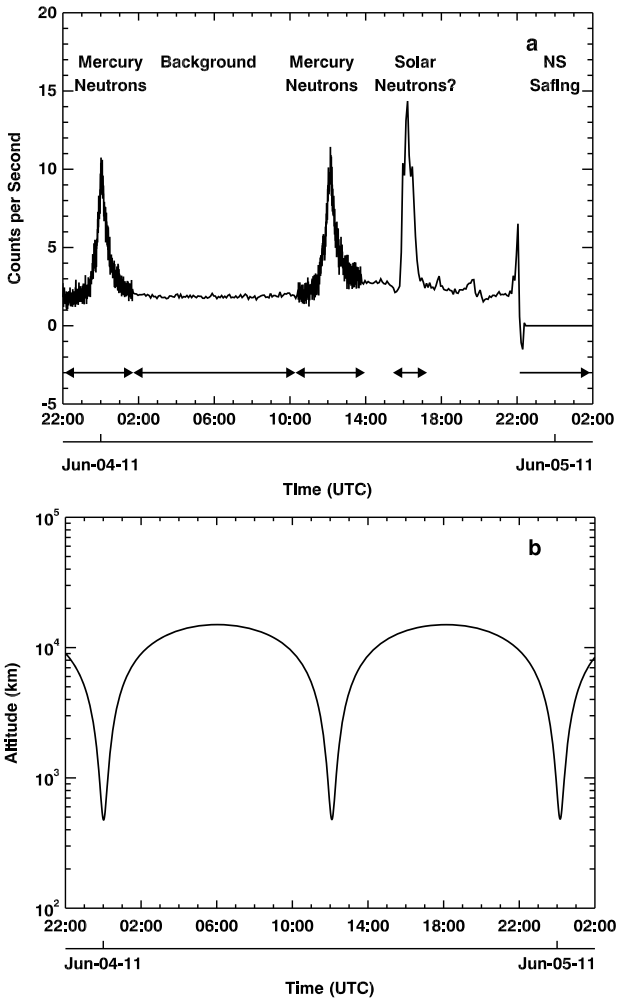

Figure 4. (a) Count rate of fast neutrons having energies ranging from 0.5 to 10 MeV detected by the MESSENGER NS. Times of several events are shown in the figure. (b) MESSENGER spacecraft altitude at Mercury for the same time interval as in Figure 4a.

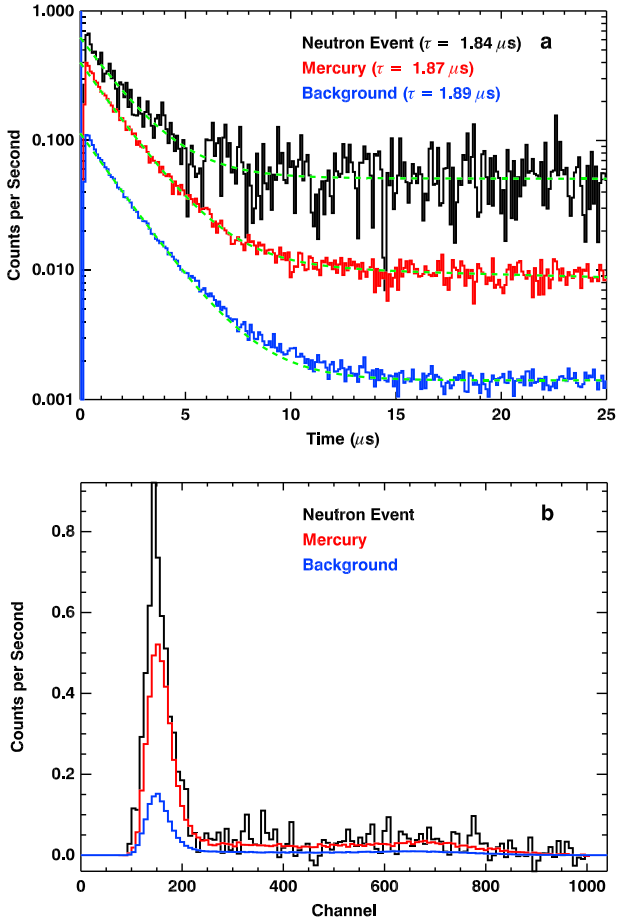

Figure 5. NS fast-neutron event mode data taken during the 4 June 2011 event (black line), a Mercury periapsis passage (red line), and a background period (blue line). (a) TTSP histogram. (b) Second pulse histogram. The dashed green line in Figure 5a shows a double-exponential fit to the TTSP data. The fitted exponential decay times for the early fast-neutron portion of the histogram are indicated. The peak at channel 150 indicates a positive detection of neutrons from the ^{10}B (n,α) reaction in the BC454 scintillator.

including the time from 15:45 to 16:45 UTC. The magnitude of the late-time portion of the distribution gives a measure of the accidental count rate within the full 25 μs coincidence window. The neutron event shows an enhanced accidental count rate compared with the other time periods and indicates a higher count rate of nonneutron particles onto the NS. The net fast neutrons (Figure 4) were determined by subtracting the late-time count rate from the early-time count rate.

[11] A histogram of the second pulse, the result of the ^{10}B(n,α) reaction, versus NS channel is shown in Figure 5b. In all three time periods, the peak at channel 150 indicates the electron-equivalent energy deposition of 93 keV from the ^{10}B(n,α) reaction and provides additional evidence for the clean detection of fast neutrons in all three time periods.

[12] Another count rate enhancement observed near 22:00 UTC is followed by an abrupt shift to a baseline level (Figure 4a). As discussed in section 4, this enhancement corresponds in time with the arrival of a large flux of energetic charged particles. Soon after the arrival of the charged particles, the count rate in the NS scintillator became sufficiently large that the autonomous safe mode was triggered and the high voltage for the borated plastic (BP) photomultiplier tube (PMT) was lowered.

[13] In summary, the MESSENGER NS was operating nominally during 4 June 2011 until 22:00 UTC and collecting planet-generated and background fast-neutron data. At 15:45 UTC, there was a clear, 1-h-long enhancement of positively identified fast neutrons not associated with Mercury. This enhancement preceded the arrival of a large flux of charged particles by approximately 6 h.

4. Evidence for a Solar Origin of Neutrons Detected at 15:45 UTC

4.1. Charged-Particle Measurements

[14] The MESSENGER NS has three scintillators—one borated plastic (BP) and two lithium glass (LG1 and LG2)—that can operate as a simple charged-particle telescope [*Feldman et al.*, 2010]. There are three types of NS events that provide a measure of charged particles. These are BP and LG singles events, BP-LG1 or BP-LG2 double-coincidence events, and BP-LG1-LG2 triple-coincidence events. At present there is currently no capability to distinguish between energetic electrons and ions. The minimum energy thresholds to trigger the three types of events were initially estimated by *Feldman et al.* [2010]. With revised particle transport code simulations, we have updated these minimum energy thresholds to the following: singles, 15–30 MeV protons (or 1 MeV electrons); double coincidences, >45 MeV protons (or >10 MeV electrons) on the basis of half-maximum count rates for an isotropic energetic particle flux; and triple coincidences, >125 MeV protons (or >30 MeV electrons).

[15] Singles and coincidence count rates are shown as functions of time in Figures 6 and 7, respectively. These figures illustrate a number of points. Close approaches to

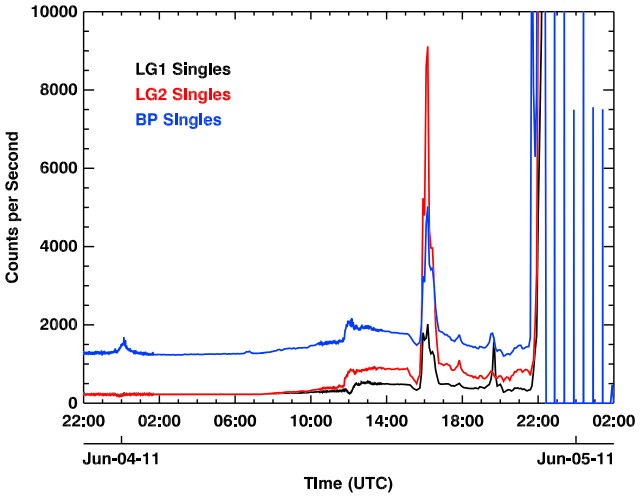

Figure 6. Dead-time-corrected singles count rates from the three NS sensors: LG1 (black line), LG2 (red line), and BP (blue line).

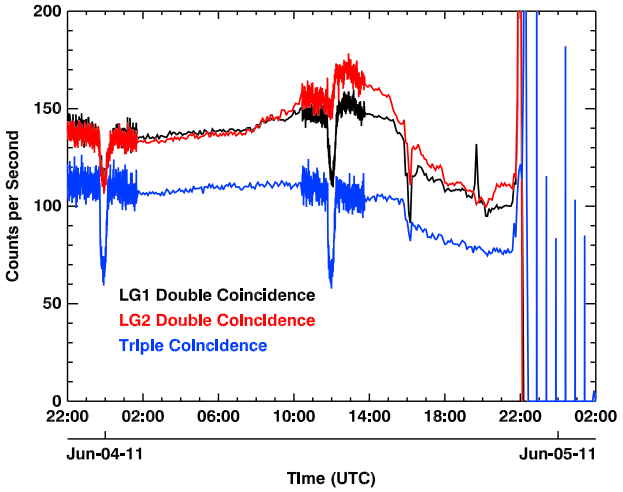

Figure 7. Dead-time-corrected NS coincidence count rates.

Mercury have little effect on the singles count rates, but they result in marked decreases in the coincidence count rates. The reason for this decrease is primarily geometric shielding of spacecraft-incident GCRs by Mercury, an effect indicating that GCRs comprise a sizeable portion of the coincidence signals. We also note relative differences in the LG1 and LG2 count rates (both singles and coincidences), which may be due to differing viewing geometries of the received radiation (the LG1 and LG2 sensors are blocked by different amounts of spacecraft material) and/or slight variations in the gains of the LG PMTs relative to their respective electronic thresholds. We have not yet achieved a fully quantitative understanding of the relative differences in these counting rates.

[16] The singles count rates show an enhancement around the time of Mercury's closest approach and a strong enhancement during the same time as the fast-neutron enhancement of 15:45 UTC. The double-coincidence signals show a slight enhancement of ~15–35 cps starting at approximately 08:00 UTC and extend through a Mercury closest approach; this increase may be related to the CME indicated by the STEREO-A energetic particle data. The triple-coincidence signal does not show a measurable enhancement. Neither the double- nor triple-coincidence signals show any evidence of strongly enhanced count rates during the time of the neutron event. At a maximum, the LG2 double-coincidence count rate rises slightly at the beginning of the neutron event by no more than 5 cps. In addition, the coincidence count rate shows a slow decrease from around 15:00 UTC to 21:00 UTC. In the middle of the fast-neutron event, the coincidence counts do show a decrease for a single 300 s data accumulation period. This decrease is likely the result of an imperfect dead-time correction to the coincidence counters. Further details about the dead-time correction are given in Appendix A.

[17] Between 21:00 and 22:00 UTC, there was a sharp rise in all count rates. Soon after 22:00 UTC, the NS BP sensor entered into an autonomous safe mode whereby the high voltage (HV) on the BP PMT was lowered to protect the PMT. The BP raw count rate threshold (not dead-time corrected) for entering safe mode was 50,000 cps. The half-hour-cadence count rate spikes after 22:00 UTC corresponded to times when the NS autonomously raised the HV to briefly ascertain if the count rate had lowered to a level safe for the PMTs. The NS halted autonomous attempts to reenable the HV at 10:30 UTC on 5 June 2011, indicating that the raw BP count rate continued to be above 50,000 cps for over 12 h. The BP HV was manually reenabled on 6 June 2011 at 21:00 UTC, and at that time the dead-time-corrected BP singles count rate was ~25,000 cps.

[18] From the charged-particle measurements, we may make the following observations. By themselves, the BP and LG singles enhancements observed during the fast-neutron enhancement are consistent with the detection of charged particles with energies greater than 15–30 MeV if protons and/or 1 MeV if electrons as well as gamma rays with energies greater than a few hundred keV. However, if the singles count rates were produced by gamma rays, similarly large singles count rates would be expected from Mercury-originating neutrons that have a similar neutron count rate (~10 cps). Such singles count rates are not seen when near Mercury. As a consequence, the large singles count rates allow for the presence of <45 MeV protons and/or <10 MeV electrons during the neutron event. NS singles count rates do not distinguish particle species. The absence of corresponding enhancements in the coincidence counters indicates that there was no evident increase in the flux of charged particles at energies greater than 45 MeV (protons) or 10 MeV (electrons). In contrast, at 22:00 UTC, there was a large enhancement of all count rates, which is consistent with the presence of a large flux of energetic particles, possibly both ions and electrons.

[19] As shown in Figure 3, STEREO-A observed a substantial enhancement of energetic particles on 4 June 2011. These measured fluxes can be converted into "STEREO-equivalent" double-coincidence count rates using NS double-coincidence geometry factors. Figure 8 shows energy-dependent geometry factors for energetic protons calculated by the particle transport code GEANT4; the geometry factor in Figure 8 is updated from the energy step-function geometry factor derived by *Feldman et al.* [2010]. *Feldman et al.* [2010] validated the absolute calibration of the NS double-coincidence count rate to proton flux using quiet-time measurements of GCRs. To convert the measured STEREO-A energetic particle flux to

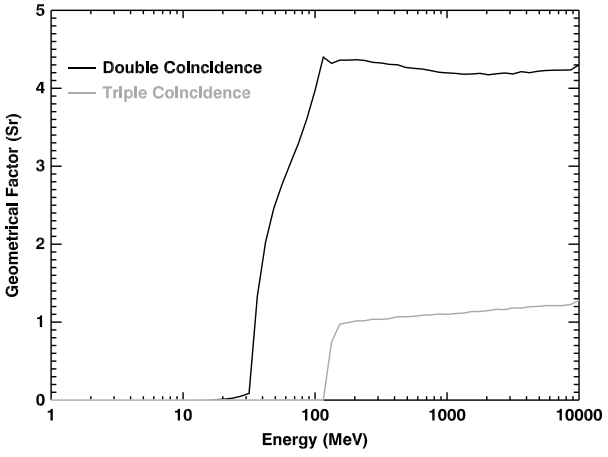

Figure 8. Geometric factor for NS double and triple coincidences from energetic protons.

equivalent double-coincidence count rates, the fluxes of Figure 3 were multiplied by the double-coincidence geometry factor and detector area of 100 cm^2 and integrated over energy. The fluxes were propagated from 1 AU to 0.32 AU using a factor of $1/0.32^2$, which is consistent with heliospheric distance scaling factors derived by *Lario et al.* [2006] for energetic protons. We find a derived STEREO-equivalent double-coincidence count rate of greater than 1000 cps during the entire time from 12:00 to 22:00 UTC. This rate is substantially larger than the 5 to 30 cps enhancement seen from the measured double-coincidence count rate in Figure 7. Thus, between 12:00 and 22:00 UTC, it appears that MESSENGER and STEREO-A were in markedly different energetic charged-particle environments, an unusual situation for pairs of locations on similar field lines [*Lario et al.*, 2013]. We also note that the MESSENGER Energetic Particle Spectrometer (EPS) detected a small count rate enhancement during the neutron event [*Lario et al.*, 2013]. This count rate enhancement, however, was only ~0.2 cps above a background value of ~0.1 cps. The 1000-μm-thick Si detectors within the EPS can respond to a variety of types of background-penetrating radiation including energetic charged particles and photons but cannot discriminate between these different types of background radiation. These data, therefore, do not provide unambiguous evidence for the presence of energetic protons.

[20] Finally, solar particle energy spectra can often be described by a power law with an exponential energy cutoff [*Ellison and Ramaty*, 1985; *Mewaldt*, 2006]:

$$F(E) = N(E+\beta)^{-\gamma}\exp(-E/E_0), \tag{1}$$

where γ and E_0 are fitted parameters and β is an offset that can be applied to the power law portion of the spectrum. Such a spectral shape has enhanced fluxes at lower energies and strongly depressed fluxes at higher energies. In principle, this type of spectral shape could provide substantial energetic ions with energies that are lower than the double-coincidence threshold (45 MeV) but sufficiently high to produce local spacecraft-generated neutrons.

[21] We investigated the feasibility of such ion energy spectra to produce neutrons from local spacecraft material by estimating the number of spacecraft-generated neutrons. Following a calculation similar to that of *Feldman et al.* [2010], we calculated the ratio of the number of neutrons generated from background GCRs to the number of neutrons generated from a solar energetic particle (SEP) spectrum. We used a ratio of count rates to reduce uncertainties associated with the absolute normalization of the incident GCR flux and a variety of transport parameters for spacecraft materials.

[22] The number of spacecraft-generated neutrons was estimated using the particle transport code MCNPX and a MESSENGER spacecraft material model [*Lawrence et al.*, 2013]. The neutron transport properties of the spacecraft model have been validated to a relative accuracy of better than 0.5% using measured GCR-generated neutrons from Mercury [*Lawrence et al.*, 2013]. The number of neutrons generated from GCRs will be different from that generated by SEPs due to the mix of different ion energies in the respective spectra. Thus, if we define S_{SEP} and S_{GCR} as the calculated neutron count rates generated from properly normalized SEP and GCR spectra, respectively, then the total estimated SEP-generated neutron count rate, C_{SEP}, can be scaled from the measured GCR-generated neutron count rate, C_{GCR}:

$$C_{SEP} = C_{GCR}\frac{S_{SEP}}{S_{GCR}}. \tag{2}$$

[23] The neutron count rate from the respective spectra can be written generally as follows:

$$S_i = A\ \Delta\Omega \int_{E_{min}}^{E_{max}} F_i(E)\Phi(E)\mathrm{d}E, \tag{3}$$

where the subscript *i* denotes either the GCR or SEP spectrum. The integral is evaluated over ion energies, E, that can produce neutrons. $F_i(E)$ is the ion energy spectrum in units of ions/(cm^2 s sr MeV) and includes separable components for protons and alpha particles. A is the NS detector area of 100 cm^2, and $\Delta\Omega$ is the solid angle of the incident ions and takes the value 4π for an isotropic distribution of ions hitting the spacecraft.

[24] The quantity $\Phi(E)$ in equation (3) is a function that incorporates neutron production, transport to the NS, and detection and is calculated with the MCNPX particle transport code. A version of this function was calculated to estimate the number of spacecraft-generated neutrons for the 31 December 2007 neutron event [*Feldman et al.*, 2010, Figure 8]. Here $\Phi(E)$ was calculated for six different orthogonal directions into the MESSENGER spacecraft as was done by *Feldman et al.* [2010]. For isotropic distributions, an average production from all six directions is used. The production function of *Feldman et al.* [2010] was critiqued by *Share et al.* [2011] for not using proper neutron cross sections for low-energy protons and alpha particles. The calculations of *Feldman et al.* [2010] used model cross sections for ion energies less than ~40 MeV/nucleon, an assumption that may have yielded underestimates of the actual neutron production. To address this shortcoming, we integrated the TALYS-based (www.talys.eu) Evaluated Nuclear Data Library (TENDL) cross sections [*Koning and Rochman*, 2012] into the MCNPX code. Specifically, we used the TENDL values for ion energies less than 200 MeV/nucleon, which is the highest energy provided by the TENDL cross sections. For higher energies, we used the standard cross section libraries provided by MCNPX. We explicitly included all material isotopes of interest that may produce measurable neutrons, including ^{13}C, which was highlighted by *Share et al.* [2011] as being able to produce abundant neutrons from low-energy ions.

[25] To normalize the GCR proton and alpha particle spectra, we used the parameterization of *McKinney et al.* [2006] and chose an appropriate solar modulation parameter. For a solar modulation parameter of 350 MV and a neutron energy threshold of 2.5 MeV, a value used by *Feldman et al.* [2010], we find $S_{GCR} = 0.6$ cps, which is only 20% higher than the 0.5 cps count rate reported by *Feldman et al.* [2010] for GCR-generated neutrons in the late 2007 time frame.

[26] The SEP spectra were normalized using the measured double-coincidence counts and the assumption that double-coincidence count rate enhancements are due only to energetic ions. Since energetic electrons can contribute to the double-coincidence count rate, the equality given in equation (2) should be an inequality written so that C_{SEP} represents an upper limit on the SEP-derived neutron count rate.

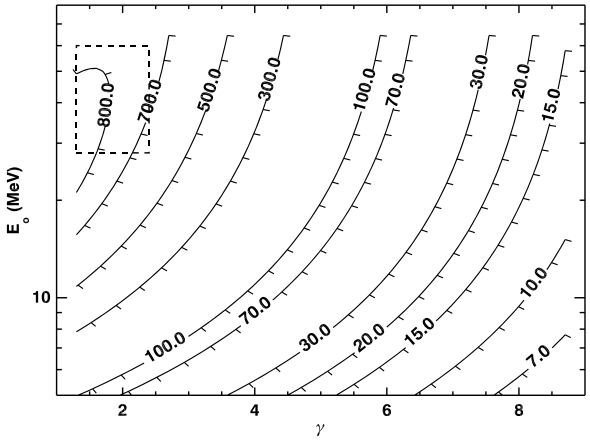

Figure 9. Contour plot of the ratio of measured neutrons, C_{EVT}, to estimated SEP-generated neutrons, C_{SEP}, for the 4 June 2011 neutron event as a function of SEP spectral parameters γ and E_0. The dashed box at upper left shows the range of γ and E_0 values for various reported SEP spectra.

By means of a process similar to that used to derive STEREO-equivalent double-coincidence count rates, the measured double-coincidence signal, C_{DBL}, can be used to normalize SEP spectral shape:

$$C_{DBL} = N_{SEP} A \int_{E_{min}}^{E_{max}} \Omega_{DC}(E) F_{SEP}(E) dE, \quad (4)$$

where $\Omega_{DC}(E)$ is the energy-dependent solid angle function of the NS double-coincidence signals (Figure 8) and N_{SEP} is the normalization factor that is directly calculated with the known quantities of equation (4).

[27] Equation (2) may be evaluated for an adopted shape of the SEP spectrum of the form of equation (1) along with an assumed ratio of alpha particles to protons of 0.02. Following *Feldman et al.* [2010], we used $\gamma = 2.41$, $E_0 = 62.5$ MeV, and $\beta = 0.12$ MeV. For C_{DBL}, we used 5 cps, which is the upper range of an LG2 double-coincidence count rate enhancement immediately prior to the neutron event. We note that this double-coincidence count rate is itself an upper limit, as no enhancement was clearly discerned during the neutron event, but we used this value to place limits on the derived SEP-generated neutrons. For $C_{GCR} = 2.7$ cps as the background neutron count rate (Figure 4a), we find $C_{SEP} < 0.013$ cps. The measured net neutron count rate during the event, C_{EVT}, is 11.6 cps. Thus, the measured count rate is at least a factor of 725 larger than the upper limit estimated from SEP particles. A similar calculation can be carried out for the 31 December 2007 event, for which the energy range of the measured neutrons was chosen to range from 2.5 MeV to 8 MeV, and we adopted $C_{DBL} = 715$ cps, $C_{GCR} = 0.5$ cps, and $C_{EVT} = 1.1$ cps [*Feldman et al.*, 2010]. With these parameters, we find $C_{SEP} < 0.41$, which compares with the value of 0.20 given by *Feldman et al.* [2010]. The ratio of measured neutrons to estimated SEP neutrons for the 31 December 2007 event obtained here is smaller (2.65) than the prior value (5.4) given by *Feldman et al.* [2010]. Although this difference from the *Feldman et al.* [2010] ratio may be attributed in part to the improved cross sections, other modifications to this calculation (e.g., energy-dependent solid angle factor in equation (4) and an improved transport model through the spacecraft to the NS) likely also contribute to the difference between the two values.

[28] Next we investigated the sensitivity of equation (2) to variations in the spectral parameters of equation (1). For example, if the cutoff energy is decreased and the power law exponent is increased, lower-energy ions will be enhanced relative to higher-energy ions. For some combination of parameters, the derived SEP production would equal that of the measured event count rate.

[29] A contour plot of the ratio $R_{EVT} = C_{EVT}/C_{SEP}$ for the 4 June 2011 event as a function of γ and E_0 is shown in Figure 9 ($\beta = 0.12$ MeV was used for these calculations). As seen, even under the conditions $\gamma > 5$ and $E_0 < 20$ MeV, R_{EVT} is no smaller than 7. *Ellison and Ramaty* [1985] reported SEP spectra for which typical values are $\gamma = 1.7$ and $E_0 = 28$ MeV. In a review study of SEP spectra, *Mewaldt* [2006] used values of $\gamma = 1.3$ and $E_0 = 31$ MeV. *Reames and Ng* [2010] reported SEP spectra from streaming-limited conditions under which the spectra have broadly peaked plateaus in the energy range 1–20 MeV. We find that these spectra (e.g., 28 October 2003) can be reasonably well fit with equation (1) using $\beta = 30$ MeV, $\gamma = 2$, and $E_0 = 60$ MeV. Finally, *Feldman et al.* [2010] used $\beta = 0.12$, $\gamma = 2.41$, and $E_0 = 62.5$ MeV on the basis of a fit to a 20 February 2002 SEP event. The dashed box in Figure 9 represents the γ and E_0 limits of these reported spectra. None of these spectra approach the combination of high γ and low E_0 values needed to produce abundant SEP-generated neutrons.

[30] Finally, it may be argued that a large flux of lower-energy charged particles (<45 MeV) from a local shock acceleration event (e.g., as reported by *Desai et al.* [1999]) could generate the required number of measured neutrons. However, multiple lines of evidence argue against such an explanation. First, the spectra observed by *Desai et al.* [1999] have γ and E_0 values ranging from 2 to 3 and 3 to 1.22 MeV, respectively. When these values are applied to extrapolated contours of Figure 9, R_{EVT} would still be more than an order of magnitude too high for the neutrons to have been locally generated. Second, if spectra of the type reported by *Desai et al.* [1999] were responsible for the measured neutrons, the proton flux in the 25 keV to 3 MeV range, which is the energy range measured by the EPS, would have been up to 8 orders of magnitude larger than the supposed proton flux with energies in the 15 to 45 MeV range. If such protons dominated the NS singles count rate, then the EPS should have also seen thousands of counts per second instead of 0.2 cps. Finally, the time profile of the event reported by *Desai et al.* [1999], which has a rise of almost 2 days and a decay of many days, is substantially different from that for the 1 h neutron event and therefore does not represent a good analogy to the neutron event. On the basis of all the reported data and analyses, we consider it unlikely that highly enhanced, low-energy SEP particles can account for the neutrons seen at MESSENGER.

[31] One final point that we investigated is the assumption made above that the SEP ions hit the spacecraft with an isotropic distribution. Under conditions of strong magnetic fields at the Sun (as was the case for 4 June 2011; see *Lario et al.* [2013]), it is possible that energetic ions may be strongly anisotropic and hit the MESSENGER spacecraft mostly from the direction of the spacecraft sunshade. In such a case, ions would have to travel through the entire spacecraft to reach

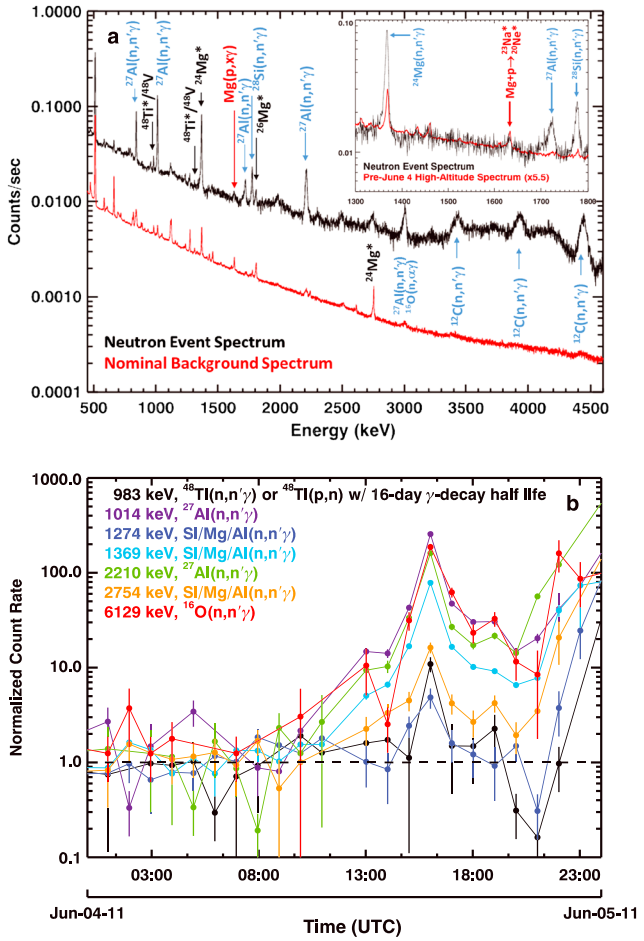

Figure 10. (a) MESSENGER GRS gamma-ray spectra measured during the neutron event (black line) and during background periods. Vertical blue labels identify gamma-ray lines produced by (n,n′γ) neutron inelastic scatter reactions. Vertical black labels identify gamma-ray lines that can be produced by both neutron inelastic scatter reactions and proton-induced reactions. Vertical red label identifies a gamma-ray line that is produced only by a proton-induced reaction. Inset to Figure 10a shows energies from 1300 to 1800 keV with the background spectrum scaled to the neutron event spectrum. A large increase in various neutron inelastic scatter lines is seen; no increase is seen for the 1635 keV line from the proton-induced reaction. (b) Background-subtracted gamma-ray count rates for various neutron inelastic scatter gamma rays as measured with the MESSENGER GRS. The time period when the MESSENGER spacecraft was close to Mercury has not been included for the sake of clarity.

the NS. Some fraction of these ions that are above the energy threshold of the NS double coincidence would likely be stopped and would not be registered by the double-coincidence counts. We have not carried out a full three-dimensional mapping of the stopping power for the MESSENGER spacecraft. However, we modified the calculations above to include only those SEP ions that hit the spacecraft from the sunshade direction. Under that geometry, the ratio R_{EVT} is a factor of 5 to 10 larger than that given in Figure 9. Thus, even if the double-coincidence signals were missing some highly directional, low-energy-enhanced ions, a combination of unusual spectral parameters would still be needed to produce the neutrons observed for the 4 June 2011 event.

[32] In summary, when all the information is combined from the singles and coincidence count rates, we find that these count rates are inconsistent with the presence of fluxes of charged particles so high as to produce locally generated neutrons with the measured neutron count rate. As a consequence, the charged-particle data and neutron production modeling imply that the fast neutrons seen at 15:45 UTC are most likely of solar origin.

4.2. Gamma-Ray Measurements

[33] The MESSENGER spacecraft carries a Gamma-Ray Spectrometer (GRS) for measuring Mercury's surface elemental composition by the detection of characteristic-energy gamma rays from the surface. The MESSENGER GRS consists of a cryogenically cooled, high-purity Ge sensor surrounded by a borated plastic anticoincidence shield [*Goldsten et al.*, 2007]. To preserve the limited-lifetime mechanical cooler, the GRS was operated only briefly during the interplanetary cruise phase of the mission (see Figure 1), and no GRS measurements were made during the 31 December 2007 event from which measurements of solar neutrons were reported [*Feldman et al.*, 2010]. In contrast, the 4 June 2011 event occurred during nominal Mercury orbital operations, and the GRS returned full gamma-ray spectra for the event. During orbital operations, the GRS had a data collection time cadence of 60 s when near Mercury (altitude less than 6000 km) and 3600 s when far from the planet. Examples of gamma-ray spectra taken during the Mercury primary orbital mission have been given by *Peplowski et al.* [2011, 2012] and *Evans et al.* [2012].

[34] An average gamma-ray spectrum during the neutron event is shown in Figure 10a. This figure also shows a gamma-ray spectrum taken during a nominal background period. As seen, there are many particle-induced gamma-ray lines, including lines that are produced both by (n,n′γ) and (p,xγ) channels (where x represents various other reaction products). These line enhancements are consistent with gamma-ray production by neutrons and protons hitting spacecraft material that contains large amounts of carbon, aluminum, and magnesium [*Goldsten et al.*, 2007; *Evans et al.*, 2012].

[35] There is at least one line at 1635 keV that can be produced only by a proton-induced reaction: Mg(p,xγ_{1635}). This line is seen during background periods (from GCR protons) as well as during the neutron event. However, this line has no enhanced count rate during the neutron event (see inset to Figure 10a). The lack of such an enhancement can be used to set quantitative limits on the number of <45 MeV protons that could have been present during the neutron event. If the measured neutrons were locally produced, then all of the enhanced (n,n′γ) lines would be ultimately due to protons hitting the spacecraft, including the 1369 keV Mg(n,n′γ) line, which has an average production cross section of ~400 mb for neutron energies less than 20 MeV [*Kim et al.*, 2007]. This line can also be produced from elements other than Mg (e.g., Al and Si), but the GRS sensor is surrounded by a Mg housing, and other estimates suggest that Mg will likely contribute at least 50% of the overall neutron reactions [*Reedy*, 1978]. Cross sections for the proton-induced Mg(p,xγ_{1635}) reactions have a mean value of ~150 mb for

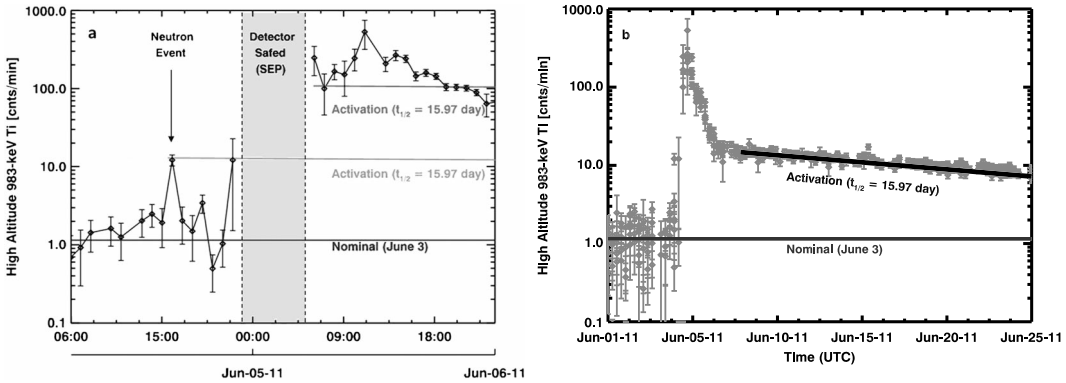

Figure 11. Time variation of the 983 keV gamma-ray line, which is excited by both neutron inelastic and proton-induced reactions. (a) The time of the neutron event is labeled, and the immediate times around 5 June 2011 are shown. The gray zone shows when the GRS was turned off because of a large flux of energetic particles. (b) An expanded time range where the activation of the 983 keV line is clearly seen.

proton energies above the reaction threshold and less than 45 MeV [*Lesko et al.*, 1988]. Thus, the gamma-ray production per incident source particle will be approximately a factor of 5 larger for the (n,n′γ_{1369}) neutrons than for the (p,xγ_{1635}) protons. Next, we investigate the relative number of source particles. On the basis of the work of *McKinney et al.* [2006], the number of spallation neutrons per incident proton is highly energy dependent and has a value of 1 for a proton energy of 300 MeV. From relative values given by *Feldman et al.* [2010], the neutron production for proton energies less than 45 MeV will be on the order of 0.01 neutrons per proton or less. This value may be conceivably higher by up to a factor of 2 because of enhanced low-energy production on some target isotopes [*Share et al.*, 2011] (see also section 4.1). As a consequence, for every neutron that creates a gamma ray from the Mg(n,n′γ_{1369}) reaction, there should be at least 50–100 protons. On the basis of the relative cross sections, these protons should produce 10 to 20 1635 keV gamma rays from the Mg(p,xγ_{1635}) reaction for every 1369 keV Mg gamma ray. During the neutron event, the 1369 keV gamma-ray line is a factor of 40 above the nominal cruise value (Figure 10b). Thus, the measured 1635 keV line should have shown a factor of 400 to 800 increase if protons less than 45 MeV were producing local neutrons. Such an increase is clearly not seen. As a consequence, these gamma-ray data provide strong, independent evidence that there were few-to-no energetic protons present during the neutron event at MESSENGER.

[36] The time variations of selected gamma-ray lines for altitudes greater than 5500 km are shown in Figure 10b. Each of the data points represents a 3600 s data collection period, and each color represents the count rate of a specific gamma-ray line. The gamma-ray lines shown are the strongest lines in the GRS spectra and are dominated by spacecraft-originating gamma-ray emission. As stated above, each is the known product of one or more neutron inelastic scatter reactions with MESSENGER spacecraft materials [e.g., *Goldsten et al.*, 2007]. For the time period of the fast-neutron event each of the gamma-ray lines shows a marked count rate enhancement.

[37] Further information from gamma-ray data is shown in Figure 11. Figure 11a shows the count rate of the 983 keV gamma-ray line during the second half of 4 June and all of 5 June. This 983 keV line can be produced from three different reactions. First, it can be produced by prompt ^{48}Ti(n,n′γ) and ^{48}Ti(p,p′γ) inelastic scatter reactions, which have no long-term activation. It can also be produced during the decay of ^{48}V to ^{48}Ti; ^{48}V is created by the ^{48}Ti(p,n)^{48}V proton reaction and has a 16 day half-life. The MESSENGER spacecraft fuel tanks, which are made from titanium, are located close to the GRS and can therefore provide an adequate concentration of titanium atoms to produce all types of 983 keV gamma-ray lines.

[38] As seen in Figure 11a, at the time of the neutron event there was a strong enhancement of the 983 keV line. After the fast-neutron event and prior to the arrival of the energetic protons, the 983 keV count rate returned to a level consistent with its value before the neutron event count rate. At 22:00 UTC, the GRS went into a safe mode in a manner similar to the NS. Both before and after the safe mode, there was an elevated 983 keV count rate that was coincident with the presence of elevated levels of solar energetic charged particles. After the safe mode and the end of the proton event, the 983 keV count rate decayed with a time characteristic of a 16 day half-life (Figure 11b), conclusively demonstrating that the ^{48}Ti(p,n) reaction occurred within the spacecraft and produced ^{48}V ($t_{1/2}$ = 15.9 days). The post-22:00 UTC gamma rays are therefore dominated by proton-induced gamma rays.

[39] The lack of delayed 983 keV gamma rays following the neutron event, but before the proton event, can be used to constrain the amount of protons present during the neutron event. Specifically, we can test the hypothesis that <45 MeV protons were responsible for producing the neutrons during the neutron event. We first note that in the energy ranges of interest, the average cross sections to produce the various gamma rays are ~400 mb for the ^{48}Ti(n,n′γ) reaction, ~30 mb for the ^{48}Ti(p,p′γ) reaction, and ~200 mb for the ^{48}Ti(p,n)^{48}V reaction [*Kim et al.*, 2007; *Brown et al.*, 1986; *Michel et al.*, 1978]. On the basis of the reasoning given above, if low-energy protons produced the local neutrons, then the number of protons per neutron will be a factor of 50 to 100. If this is the case, then from the respective cross sections, there will be a factor of 5.3 to 5.9 more reactions that produce the delayed gamma rays than prompt gamma rays (400 mb + 30 mb × [50 to 100] for prompt versus 200 mb × [50 to 100] for delayed). The number of counts as a function of time, t, for the delayed gamma rays is $A(t) = \lambda N_0 \exp(-\lambda t)$, where $\lambda = 0.693/t_{1/2}$, and $t_{1/2}$ = 15.97 days. N_0 represents the total

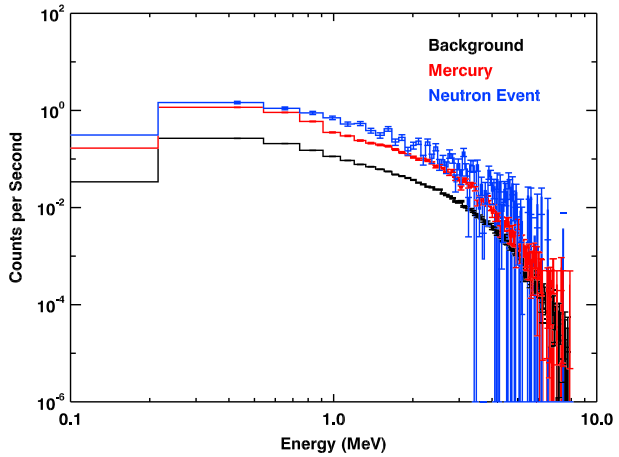

Figure 12. NS fast-neutron energy spectra measured with the prompt BP signal. Spectra are shown for a background region from data prior to 4 June 2011 09:29 UTC and for Mercury altitudes greater than 8000 km (black line), for the Mercury periapsis passage on 4 June 2011 near 12:00 UTC (red line), and for the neutron event (blue line). Error bars give the statistical uncertainty. For the lower-energy data, the error bars are similar in size to the line thickness.

number of ^{48}Ti(p,n)^{48} V reactions during the neutron event. The measured 983 keV count rate during the event is 12.5 counts per minute or 750 counts per day. Under the hypothesis that the measured neutrons were produced by low-energy protons, we can apply the 5.3 to 5.9 scale factor to derive an N_0 value from ^{48}Ti(p,n)^{48} V reactions of 3975 to 4425. This value can then be compared with the observed delayed 983 keV count rate following the neutron event. The lowest count rate after the neutron event was 0.5 ± 0.23 counts per minute, and this value was seen approximately 5 h after the neutron event. For $t = 5$ h $= 0.21$ day, $A(t) = 171$ to 190 counts per day or 0.12 to 0.13 counts per minute. On the day prior to the neutron event (June 3), the average high-altitude 983 keV count rate was 1.14 counts per minute. The net delayed 983 keV count rate is therefore constrained by $(0.5 + 0.23\sigma) - 1.14 = 0.12$ to 0.13 counts per minute, where σ represents the number of standard deviations required to reach the hypothesized delayed count rate. Solving for σ gives values of 3.30 to 3.35, values sufficiently high as to argue against the hypothesis that <45 MeV protons produced local neutrons during the neutron event.

4.3. Summary of Evidence for a Solar Origin of the Neutrons at 15:45–16:45 UTC: Neutrons, Charged Particles, and Gamma Rays

[40] The NS detected a clear enhancement of fast neutrons from 15:45 to 16:45 UTC. Since the MESSENGER spacecraft was at an altitude greater than 8000 km at the time, these neutrons were not associated with Mercury, as GCR-generated planetary neutrons can be detected only when the spacecraft is approximately within one Mercury radius (2440 km) of the surface. NS scintillator count rate data show a singles count rate enhancement coincident in time with the fast-neutron enhancement. However, the double- and triple-coincidence count rates show no enhancement. This lack of coincidence count rates coupled with neutron production models constrain the type of energetic ion spectra that could produce local neutrons to very soft ion spectra, which have not been reported; we therefore consider the presence of such ion spectra during the neutron event to be unlikely. Gamma-ray spectral measurements are consistent with this interpretation, as these data show an enhancement of multiple inelastic scatter gamma-ray lines that are coincident in time with the fast-neutron enhancement. In addition, there is no enhancement of a proton-induced gamma-ray line, which would be expected if there were an enhanced energetic proton flux at the MESSENGER spacecraft. Finally, the 983 keV gamma-ray line argues against an enhanced proton flux during this time to greater than a three-standard-deviation level. In summary, the data are consistent with the conclusion that there was no enhancement of energetic protons at MESSENGER during the time of the fast-neutron event sufficiently large to produce local neutrons. The absence of these energetic protons makes it highly unlikely that there would be energetic alpha particles, as their fluence relative to protons is generally less than 20% [*Mewaldt*, 2006]. Since the totality of the data show that there were few to no energetic ions available to produce neutrons from local spacecraft material, we conclude that the detected neutrons were most likely produced at the Sun.

5. Neutron Energy Spectra

[41] The NS provides a broad energy measurement for neutrons incident on the NS via the prompt pulse of the BP double-pulse interaction. *Hua et al.* [2002], and more recently *Murphy et al.* [2012], calculated the expected shape and magnitude of energy fluence spectra from solar events. *Murphy et al.* [2012] calculated energy fluence spectra in response to the prior report of low-energy solar neutrons by *Feldman et al.* [2010] and explicitly accounted for lower energy neutrons that may be detectable by the MESSENGER NS. In this section, we derive a neutron energy spectrum at Mercury and compare it with predictions from a forward model to understand the spectra measured by the NS. The forward model is validated with an input energy spectrum from Mercury that has a known spectral shape. The validated model is then used to investigate the measured spectral shape of the solar neutrons and compare it with the predicted input fluence spectrum from *Murphy et al.* [2012].

5.1. MESSENGER NS Measurements

[42] The channel-to-energy scale and energy spreading of the NS were quantified from prelaunch calibration data (Appendix B). The measured energy spectra for non-Mercury background, Mercury, and the solar neutron event are shown in Figure 12. The flight NS has an event-mode data collection during which a full 16 bit channel resolution (65,536 channels) can be obtained. However, to show a statistically significant count rate in each channel, the spectra in Figure 12 are binned into 128 channels, and the horizontal axis channels are labeled with the corresponding energies as calculated from equations (B1) and (B2). The average background spectrum has been taken from 3 June 2011 00:00 UTC to 4 June 2011 09:30 UTC and excludes times when the MESSENGER spacecraft was within 8000 km of Mercury's surface. These background neutrons are created from spallation reactions induced by GCRs hitting spacecraft material. The average spectrum from Mercury has been taken from MESSENGER's closest approach to Mercury at 12:00 UTC on 4 June 2011

UTC and includes all spectra acquired when the spacecraft was within one planetary radius of the surface. Finally, the solar neutron spectrum is the count-averaged spectrum for the 1-h-long neutron event starting at 15:45 UTC on 4 June 2011. The error bars show the statistical uncertainty for each channel.

[43] The shapes of all spectra are generally similar, a consequence of both the moderation of neutrons within spacecraft material and the energy spreading of the NS (see sections 5.3 and 5.4). Despite the overall similarities, notable differences in spectral shapes are seen. The Mercury neutron spectrum falls off more quickly at higher energies than both the GCR background and the solar neutron spectrum, although the limited high-energy statistics make this conclusion less definitive for the solar neutrons. The solar neutron spectrum shows a statistically significant enhancement in the mid-energy range ~0.8 to ~3 MeV, a result indicating that the spacecraft-incident neutrons from the event may have a different shape from that of the Mercury neutrons. In the following subsections, we describe a spectral forward model that allows us to investigate the degree to which the Mercury and solar neutron spectra can be characterized and discriminated.

5.2. Neutron Spectrum Forward Model

[44] Here we present a forward model of input neutrons with a given energy spectrum that are incident on the front of the MESSENGER spacecraft and are then propagated through the spacecraft materials to the NS. The goal of the forward model is to account for the particle transport and detection processes by accurately reproducing the shape of the measured spectra following moderation in the spacecraft. Information about the source magnitude of the input spectrum can also be obtained through this forward model calculation.

[45] The measured count rate spectrum, C, is initially defined as a function of channel, x, where the channels represent the full 16 bit channel resolution of the NS prompt-pulse measurement,

$$C(x) = F(x)\mathrm{d}x, \tag{5}$$

and where $F(x)$ is the count density (counts per channel) as a function of channel. In calculating the forward model, we work in energy space rather than channel space. However, note that in Figure 12, although the horizontal axis is labeled as energy, the measured channel counts have not been transformed to energy space so as to show the counts that are actually measured in the NS. Because the integrated counts over energy and channel are the same, the differential counts in channel and energy space are also equal:

$$F(x)\mathrm{d}x = NF(E_\mathrm{t})\mathrm{d}E_\mathrm{t}. \tag{6}$$

Here E_t is the energy incident on the NS that has been transported through the spacecraft, $F(E_\mathrm{t})$ is defined as a normalized incident neutron flux on the NS, and N is a generalized normalization constant. From equation (6), the measured count rate can be expressed in terms of the incident neutron flux:

$$C(x) = NF(E_\mathrm{t})\frac{\mathrm{d}E_\mathrm{t}}{\mathrm{d}x}\mathrm{d}x. \tag{7}$$

[46] The differential, $\mathrm{d}E_\mathrm{t}/\mathrm{d}x$, is calculated from equation (B1):

$$\frac{\mathrm{d}E_\mathrm{t}}{\mathrm{d}x} = a'bx^{b-1}, \tag{8}$$

where a' and b are given in Appendix B.

[47] The flux function, $F(E_\mathrm{t})$, is determined as an integral of the neutron fluence incident on the spacecraft over the spacecraft-incident energy, E:

$$F(E_\mathrm{t}) = \int_{E=0.5\ \mathrm{MeV}}^{9\ \mathrm{MeV}} Q_n(E)D(E)T(E,E_\mathrm{t})A\varepsilon(E_\mathrm{t})\Delta\Omega\mathrm{d}E \tag{9}$$

where $Q_\mathrm{n}(E)$ is the neutron fluence at the Sun or Mercury, and other quantities are defined below. The units of neutron fluence given by *Murphy et al.* [2012] are neutrons $\mathrm{MeV}^{-1}\,\mathrm{sr}^{-1}$ produced by protons having energies greater than 30 MeV. Therefore, when using the *Murphy et al.* [2012] fluence, the normalization constant will have units of (protons with energy >30 MeV).

[48] The quantity $D(E) = \exp[-t(d)/\tau]$ in equation (9) accounts for the decay of the neutrons from the Sun to Mercury, where $t(d)$ is the neutron travel time over a distance d and $\tau = 886$ s is the mean neutron lifetime [*Nieto et al.*, 2008]. For lower energy neutrons, it is appropriate to calculate the travel time with a nonrelativistic approximation so that

$$t = \frac{1.09\times10^4 d}{\sqrt{E}}, \tag{10}$$

where d is expressed in units of AU and E is expressed in units of MeV. The neutron decay is then

$$D(E) = \exp\left(-12.2d/\sqrt{E}\right). \tag{11}$$

[49] On 4 June 2011, the distance of the MESSENGER spacecraft from the Sun was $d = 0.32$ AU.

[50] The quantity $T(E,E_\mathrm{t})$ in equation (9) is a neutron transmission function and accounts for the moderation, scattering, and absorption processes of the neutrons as they travel through the spacecraft material to the NS. Appendix C describes $T(E,E_\mathrm{t})$ and how it is calculated.

[51] The quantity $A\varepsilon(E_\mathrm{t})$ in equation (9) is the area/efficiency product of the NS for fast neutrons and was calculated for the NS with MCNPX in a manner similar to that done for a comparable borated plastic fast-neutron detector on the Dawn spacecraft [*Prettyman et al.*, 2011]. The area, A, of the NS is 100 cm^2. Finally, $\Delta\Omega$ in equation (9) is the solid angle of a 1 cm^2 area at distance $d = 0.32$ AU from the Sun: $\Delta\Omega = 1/d^2 = 4.3\times10^{-26}$ sr.

5.3. Application of the Forward Model: Neutrons From Mercury

[52] Before applying the forward model for neutron spectra to the case of solar neutrons, we first validated it with a known input neutron energy spectrum, namely, the neutron spectrum from Mercury. The purpose of this validation is primarily to show that the measured spectral shape can be accurately reproduced with a known input spectral shape. This validation demonstrates that the spacecraft geometry, neutron transport, and detection physics are properly taken into account and will provide confidence in the application of the forward model to study solar neutrons.

[53] We started with equation (9) and defined each term for the case of Mercury neutrons. Here $Q_\mathrm{n}(E)$ is the incident neutron flux from Mercury as produced by GCRs. If the surface elemental composition is known, then the shape of the resulting neutron flux spectrum can be calculated with

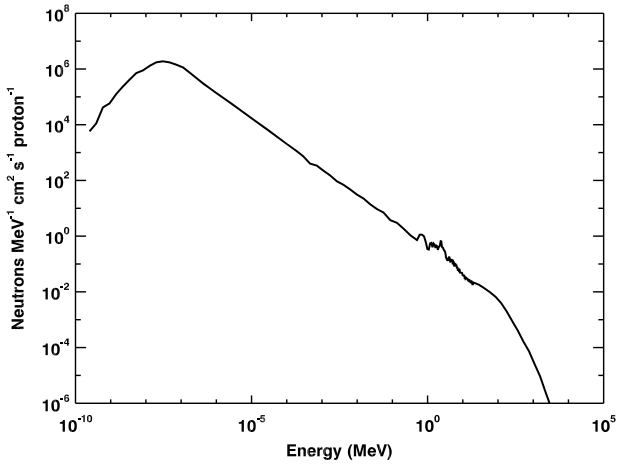

Figure 13. Neutron energy spectrum from Mercury calculated using MCNPX and Mercury surface elemental compositions.

particle transport codes. The results of these particle transport codes have been validated with neutron number density measurements on Apollo sample drill cores [*McKinney et al.*, 2006] and from orbital neutron measurements at Mars [*Prettyman et al.*, 2004], the Moon [*Lawrence et al.*, 2006], and Mercury [*Lawrence et al.*, 2010, 2013]. Validation of in-space energy spectra of GCR-generated neutrons has been completed for a borated plastic scintillator similar to that in the MESSENGER NS, namely, that on the Mars Odyssey spacecraft [*Feldman et al.*, 2002]. The simulated neutron flux spectrum from Mercury, shown in Figure 13, was calculated with a full-sized spherical model of Mercury using measured elemental compositions of Mercury's surface material [e.g., *Nittler et al.*, 2011; *Peplowski et al.*, 2011]. For the purposes of the forward model validation, the important neutron energies are those greater than 0.5 MeV.

[54] The neutron decay function, $D(E)$, was set to unity, as Mercury is sufficiently close to the spacecraft (<2000 km) that neutrons with energies greater than 0.5 MeV do not decay prior to reaching the NS. For the Mercury neutron calculation, the solid angle factor, $\Delta\Omega$, was combined with the normalization factor so as to have an overall normalization parameter. All other factors in equation (9) were used as described in section 5.2 and Appendix C.

[55] Results of the forward model are shown along with measured neutron spectra from Mercury in Figure 14. The data shown in Figure 14 are different from those shown in Figure 12 in two ways. First, near-Mercury data from 26 March 2011 to 25 February 2012 were used, but selections were made to include data only when the sunshade side of the spacecraft was facing Mercury (to within ±15°) and when the spacecraft altitude was less than 2000 km. This look-direction selection was imposed to ensure that the data used represent the same neutron input flux (i.e., input neutrons enter the front of the spacecraft) as the model tested. Second, the data in Figure 14 were binned into 1020 channels instead of the 128 channels used for Figure 12. This was done to better delineate the low-energy threshold than is possible with the 128-channel spectrum.

[56] The direct model output is shown as the dashed line in Figure 14. When the model is normalized by a factor of 35 and scaled down in energy by a factor of 0.75, the solid gray line shows the resulting modeled spectrum. The energy scale change is likely needed because of uncertainties in the original channel-to-energy calibration (Appendix B). The scaled spectrum shows a good match to the shape of the measured data, with a variety of features accurately reproduced. As an additional check on the energy scale factor, if the forward model is iterated with an initial energy scale factor of 0.75, the same match to the data shown in Figure 14 is obtained. At low energies, the threshold location is well modeled, with the main difference that the model has a sharp (and imposed) energy cutoff, whereas the measured spectrum shows a more gradual decrease consistent with the expected behavior of the NS discriminator electronics. At higher energies, the measured spectrum displays a double power law behavior with a harder spectrum up to ~2 MeV and a softer spectrum at higher energies. This spectral shape variation is represented with the modeled spectrum. One potential difference between the measurements and the model is that for the highest energies, the model slightly overshoots the data. This overestimation may reflect the possibility that the actual MESSENGER spacecraft contains more material to scatter the higher-energy neutrons than is treated in the model and/or the modeled NS efficiency is larger than for the actual detector. Notwithstanding this difference, the agreement between data and model for the case of Mercury neutrons is sufficiently robust that we can move to the case of solar neutrons with confidence that the forward model provides an accurate representation of the transport and detection of neutrons for the full MESSENGER spacecraft/NS system.

5.4. Application of the Forward Model: Solar Neutrons

[57] Neutron fluence spectra from the Sun for solar events have been modeled by *Murphy et al.* [2012], who updated the calculations of *Hua et al.* [2002] and *Share et al.* [2011]. Specifically, *Murphy et al.* [2012] included cross sections for a variety of heavy-ion reactions that would produce low-energy ($E_n < 30$ MeV) neutrons that are most easily

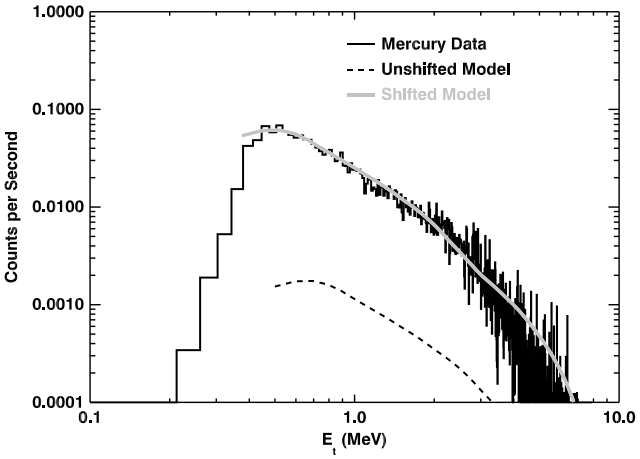

Figure 14. (black solid line) Measured neutron energy counts binned in 1020 channels that are labeled with incident energy, E_t, on the NS. (black dashed line) Modeled neutron energy spectra prior to normalization and energy scaling. (gray solid line) Modeled neutron energy spectra after applying normalization and energy scale factors.

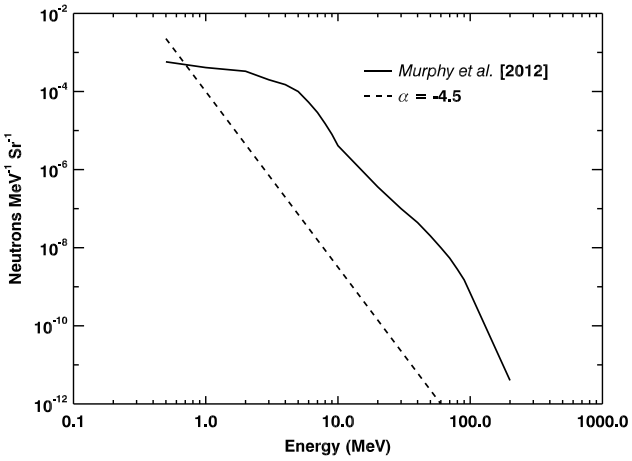

Figure 15. Input neutron fluence spectra used for the forward model. The solid line is the calculated neutron fluence from *Murphy et al.* [2012, Figure 17]. The dashed line is a power law that has a similar shape to the higher-energy portion of the Murphy et al. spectrum.

detectable by the MESSENGER NS in Mercury orbit. Here we use the fluence spectra of *Murphy et al.* [2012] as input to the forward model. Since the MESSENGER spacecraft was directly in line with the active region that produced the neutron event, we chose a modeled spectrum for which the observation angle, the angular difference in Sun-centered coordinates between the solar neutron source and the point of observation, is $\theta^{n}_{obs} = 0°$. To accentuate the low-energy portion of the spectrum, we additionally chose a neutron spectrum with an accelerated-ion spectral power law index of 6. This spectrum is the one given in Figure 17 of *Murphy et al.* [2012]. Figure 15 shows a reproduction of this spectrum.

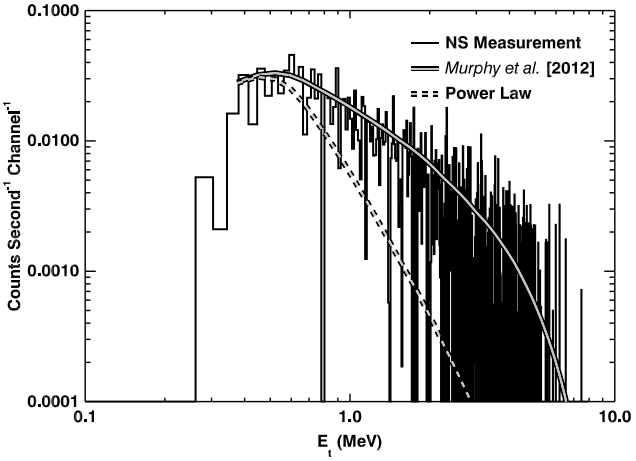

Figure 16. (black solid line) Measured neutron energy counts for the solar neutron event binned in 1020 channels that are labeled with incident energy, E_t, on the NS. (gray-black solid line) Modeled neutron energy spectrum for the *Murphy et al.* [2012] input spectrum of Figure 15. A normalization and energy shift, as in Figure 14, is applied to the modeled spectrum. (gray-black dashed line) Modeled neutron energy spectrum for the power law input spectrum of Figure 15. A normalization and energy shift, as in Figure 14, are applied to the modeled spectrum.

Shown, too, is a neutron spectrum with a power law index of 4.5, which mimics the shape of the ~10–100 MeV portion of the *Murphy et al.* [2012] spectrum. This power law input spectrum was used to test the sensitivity of the forward model to different input spectral shapes.

[58] The results of the forward model with all the input parameters and functions as described in section 5.2 are shown in Figure 16. Measured data from the solar neutron event are shown as a solid black histogram, and the modeled spectra for input spectra from *Murphy et al.* [2012] and the power law are shown as the gray-black solid and dashed lines, respectively. The same energy scale factor used in Figure 14 was also applied here, and a normalization factor was applied to each modeled spectrum in order to match the measurements at low energies. The normalized forward-modeled *Murphy et al.* [2012] spectrum clearly shows a good match to the data. In contrast, the power law model spectrum does not match the data. From this result two conclusions may be drawn. First, as with the input Mercury neutron spectrum, the input spectral shape from *Murphy et al.* [2012] can match the measured data when neutrons are propagated from the Sun to MESSENGER and then through the spacecraft material and into the NS. Second, despite the substantial spreading of neutron energy contributed by transport and detection processes, the measured energy spectra can discriminate among input energy spectra of different shapes.

[59] The degree to which the measured energy spectra can discriminate among different input spectra was further investigated by comparing the Mercury and solar neutron spectral shapes for both the measured neutrons and forward model output as illustrated in Figure 17. First, a GCR background spectrum (black line in Figure 12) was subtracted from each measured spectrum to isolate the Mercury and solar neutron portions of the measured spectra. Second, the solar neutron spectrum was normalized to the Mercury spectrum at the 200–600 keV bin so as to best illustrate differences in spectral

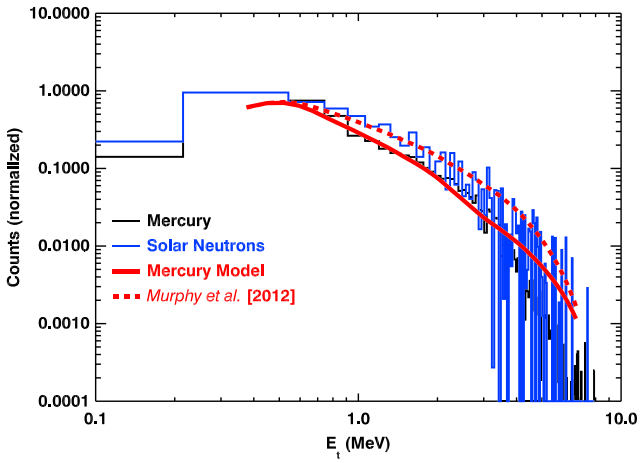

Figure 17. Measured Mercury neutron (black solid line) and solar neutron (blue solid line) count spectra binned to 128 channels as functions of energy incident on the NS. To illustrate changes in spectral shape, counts are normalized to the E_t = 200–600 keV bin. Forward-modeled spectra for Mercury (solid red line) and *Murphy et al.* [2012] (dashed red line) are self-normalized for the same low-energy portion as well as to the measured spectra.

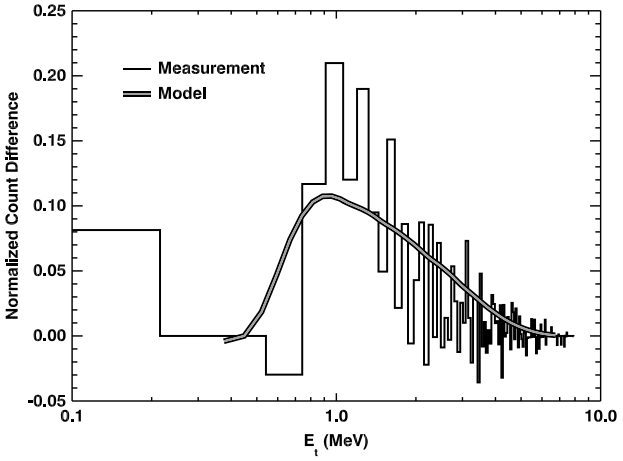

Figure 18. Count difference between the solar neutron and Mercury neutron spectra for the measurements and the modeled spectra from Figure 17; the measured difference spectrum is the solid line, and the modeled difference spectrum is the gray-black line.

shape. The modeled spectra of Figures 14 and 16 are shown as solid and dashed red lines, respectively. As with the measured spectra, the modeled *Murphy et al.* [2012] spectrum was normalized to the Mercury spectra for low energies. The modeled spectra were then normalized to the measured spectra to enable a direct comparison of spectral shapes. Both the measured and modeled spectra have similar quantitative behavior in the energy range 0.5–3 MeV, energies for which the solar spectra are enhanced relative to the Mercury spectra. We also note that the disagreement at higher energies between the Mercury model and data hinted in Figure 14 is more clearly seen here.

[60] To further illustrate the difference between the Mercury and solar neutron spectra, Figure 18 shows difference spectra between the solar neutron and Mercury spectra for both the measurements and the model. Now plotted with a linear scale for the vertical axis, there is good agreement between the measurements and the model. This result shows that at least in terms of spectral shapes, the NS data, combined with an accurate forward model, can distinguish between planetary and nonplanetary neutron spectra. In addition, Figure 18 provides further evidence that the neutrons detected at 15:45 UTC on 4 June 2011 are of solar origin, because their spectral shape is similar to that of the calculated spectral shape of *Murphy et al.* [2012].

[61] A final step in the forward model calculation is to estimate the magnitude at the Sun of the detected solar neutrons. The parameter used to scale the magnitude of solar fluence is typically the number of equivalent accelerated protons having energies greater than 30 MeV (or $N_p > 30$) needed to produce the neutrons. The *Murphy et al.* [2012] fluences were scaled in this manner, so that the normalization factor of equation (7) has units of $N_p > 30$ when the *Murphy et al.* [2012] fluence is used as input to the forward model. To determine the proton normalization factor, $N_p > 30$, equation (7) may be integrated over channels and solved for N:

$$N = \frac{\sum C(x)}{\int F(E_t(x)) \frac{dE_t}{dx}(x) dx}. \quad (12)$$

[62] In the model formulation of Figure 16, for which the model calculation was made for 1020 channels, there is an additional channel binning of the full 16 bit resolution so that $dx = 5$. The full integral in the denominator of equation (12) is calculated to be 1.9×10^{-30}. The total measured neutron counts minus the GCR background (Figure 5) is 21,000. The derived normalization factor is then 1.1×10^{34} protons with energy greater than 30 MeV.

[63] The magnitude of this normalization is the same order of magnitude as was estimated by *Share et al.* [2011] of (0.8 to 1.3) $\times 10^{34}$ for the 31 December 2007 flare, for an assumed value of the accelerated-ion power law index of 4. Our derived normalization factor is smaller than the 10^{38}–10^{40} values given by *Share et al.* [2011] when monoenergetic ions of 2 to 5 MeV are assumed. As stated by *Share et al.* [2011], all these proton normalization factors are substantially larger than one would expect for even the largest X-class flares. *Share et al.* [2011] therefore used these large normalization factors to argue against the likelihood that the neutrons detected during the 31 December 2007 event were truly of solar origin.

[64] A similar argument could be applied, in principle, to the large proton flux calculated from the 4 June 2011 event, but an alternative explanation for the observed neutron signal would then be required. Unlike the December 2007 event, which had detection ambiguities because of the presence of charged particles at the spacecraft, the strong evidence for the detection of solar neutrons on 4 June 2011 (sections 3 and 4) requires that the unexpectedly large proton normalization needs to be considered seriously. One possible way to understand the large magnitude of the derived proton normalization, which also requires a large rate of energy input, is to consider the duration of the event at the Sun. The flares modeled by *Murphy et al.* [2012] were short, impulsive flares. However, it may be that the 4 June 2011 event is a different type of solar event that has a longer duration. The measured duration of the 4 June 2011 event was ~1 h, and that of 31 December 2007 was ~5 h. If the acceleration time of protons at the Sun is spread over 1 to 5 h instead of shorter times (say 1 to 10 s), then the effective energy rate needed to generate the neutrons for longer events would be lower by 3 to 4 orders of magnitude compared with shorter-duration events. We note that the classification of flares using the GOES X-ray monitors at Earth uses X-ray intensity rather than fluence.

6. Neutron Event Timing

[65] Event timing from the Sun is another useful parameter that can be determined for the 4 June 2011 neutron event. Specifically, the timing of the neutron event compared with other time-localized solar measurements can provide additional information regarding the nature of the solar event. Solar flare events are often initiated by X-ray flashes, as was observed for the 31 December 2007 event [*Feldman et al.*, 2010]. Because the 4 June 2011 event did not occur within view of the Earth, only space-based assets on the far side of the Sun from Earth can be used for characterizing event timing. The MESSENGER X-Ray Spectrometer (XRS) includes both a Mercury X-ray Unit (MXU) and a Solar Assembly for X-rays (SAX) [*Schlemm et al.*, 2007]. The SAX was used for characterizing the X-ray timing of the 31 December 2007 event. For the 4 June 2011 event, the

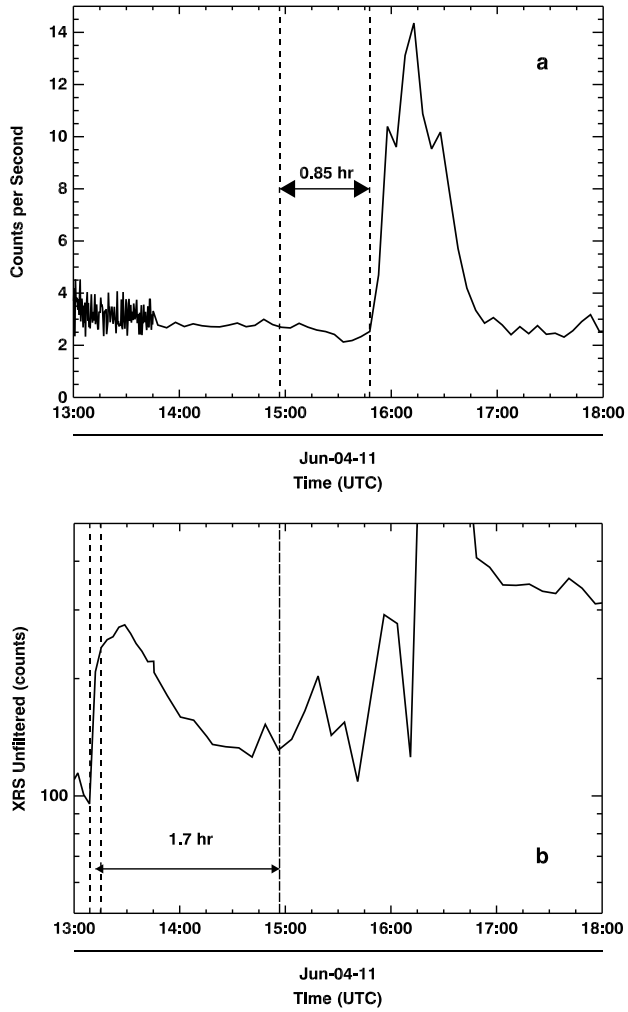

Figure 19. (a) NS fast-neutron count rate and (b) count rate from one of the three MESSENGER XRS sensors (unfiltered). The vertical dashed lines in Figure 19a show the time difference between the start of the neutron event and when a 1.25 MeV neutron would have left the Sun. The vertical dashed lines in Figure 19b show the time difference between the start of the X-ray enhancement at ~13:00 UTC and the derived solar neutron emission time shown in Figure 19a. The large XRS enhancement seen for times after 16:00 UTC are likely due to enhanced photon fluxes at the spacecraft as described in section 4.2.

MESSENGER spacecraft was orbiting Mercury during a "hot season" of nearly noon-midnight orbits, and because of high temperatures on the spacecraft the Sun-facing SAX was periodically turned off. One of the off periods for the SAX was during the 4 June 2011 neutron event. Fortunately, the planetary MXU was operating during this time and observed X-rays from Mercury. Figure 19 shows these XRS data from the unfiltered MXU sensor as a function of time; the NS fast-neutron data are also shown in Figure 19 on the same time scale as the XRS data.

[66] From the discussion of section 5.4, for a lower limit to the mean neutron energy of 1.25 MeV, the maximum neutron travel time from the Sun to the MESSENGER spacecraft was 51 min, or 0.85 h. This time difference is shown by the vertical dashed lines in Figure 19 (we have neglected the 2.7 min propagation time of the X-rays to MESSENGER). The XRS data do not show any features 0.85 h prior to the neutron event, but there was a moderate X-ray enhancement near 13:00 UTC. As shown in Figure 19, the rise of this enhancement occurred 1.7 h prior to the earliest time the neutrons would have left the Sun. Therefore, at first glance, there does not appear to be a direct causal relation between the X-ray enhancement and the neutron event.

[67] We note, however, the recent characterization of a type of solar flare event called an extreme ultraviolet (EUV) late-phase event [*Woods et al.*, 2011]. These newly recognized events were characterized with data from the Solar Dynamics Observatory EUV Variability Experiment. A specific characteristic of EUV late-phase events relevant to this discussion is the existence of hot coronal emissions that are identified with the Fe XX line that are highly correlated with GOES X-ray measurements. A coronal dimming is also observed with lines such as the Fe IX 17.1 nm line. Finally, during the posteruptive loop reconnection, warm coronal emissions (e.g., Fe XVI 33.5 nm) sometimes exhibit a second large peak separated from the main flare event by many minutes to hours. According to *Woods et al.* [2011], this emission originates "not from the original flare site and its immediate vicinity, but rather from a volume of higher loops."

[68] An interesting relation of the identified EUV late-phase events to the 4 June 2011 event is similar timing characteristics. The X-ray enhancement shown in Figure 19b is similar to the type of X-ray enhancement identified by *Woods et al.* [2011] as being correlated in time to the prompt Fe XX and He II lines. The timing of the derived solar neutron emission, which occurs no earlier than 1.7 h after the X-ray enhancement, has the same temporal pattern as the EUV late-phase emission identified by *Woods et al.* [2011]. Although a clear connection between the 4 June 2011 neutron event and EUV late-phase events is not established by these data, the timing similarities suggest that such a possibility should be investigated in more detail. The STEREO-A spacecraft did have a clear view of the 4 June 2011 event (see Figure 2). Unfortunately, on the basis of available data from the STEREO Science Center, the types of time-resolved data needed to characterize the 4 June 2011 event in terms of EUV late-phase event parameters are not available.

7. Discussion and Summary

[69] MESSENGER NS data from 4 June 2011 show strong evidence that solar neutrons were detected over a duration of ~1 h starting at 15:45 UTC. This neutron detection occurred ~6 h prior to the arrival of a large solar particle event at MESSENGER. The evidence for the solar origin of these neutrons includes the positive detection of neutrons, the absence of >45 MeV/nucleon charged ions, a lack of enhanced proton-induced gamma rays, and a positive detection of neutron inelastic scatter gamma rays. These measurements, combined with neutron production models that require very soft and unreported proton flux spectra to produce local neutrons with the measured count rate, provide strong evidence that the detected neutrons have a solar origin.

[70] Additional evidence for the solar origin of the detected neutrons is provided by the distinct shape of the solar neutron

spectrum in the energy range 0.8 to 3 MeV compared with that of neutrons detected from local GCRs or Mercury's surface. In addition, spectral forward modeling has shown that differences in input spectral shapes are distinguishable with the measured neutron energy spectra. In particular, the measured spectral shape is consistent with that of a modeled solar neutron spectral shape calculated by *Murphy et al.* [2012] that is subsequently propagated to the MESSENGER spacecraft at 0.32 AU using the 886 s mean neutron lifetime and then through the spacecraft to the NS detector. The fluence magnitude of the neutron event is substantially larger than that expected on the basis of prior estimates of solar neutron fluence magnitude derived from measurements of neutrons from large impulsive flares. The discrepancy between the inferred fluence from the 4 June 2011 event and that of prior estimates may be mitigated somewhat by attributing some of the magnitude difference to a difference in integration times of the two types of events. Finally, the time signature of the neutron event and a solar X-ray enhancement that occurred 2.5 h prior to the arrival of the neutrons at MESSENGER has similarities to recently recognized EUV late-phase events.

[71] More work, both observational and theoretical, is clearly needed to understand the full nature of this event, and detailed studies of this type are beyond the scope of this paper. Nevertheless, we offer some additional ideas to help direct future discussions. In a review of solar ion acceleration processes linked to gamma-ray and neutron observations, *Vilmer et al.* [2011] compiled and described several ion acceleration and reaction properties relevant to the 4 June 2011 neutron detection. As is generally known, heavy ions (atomic number $Z > 1$) can be prolific producers of free neutrons through low-energy threshold evaporation reactions [e.g., *Murphy et al.*, 2012]. According to *Vilmer et al.* [2011] (and also *Murphy et al.* [2007]), softer energy spectra and low-energy threshold reactions occur in lower-density environments than interactions with higher-energy thresholds, which occur preferentially in higher-density environments. Finally, *Vilmer et al.* [2011] stated that "The content in low-energy ions from flares is mostly unknown and no strong constraints have been derived on the production of low-energy protons in solar flares."

[72] Although a direct link has not been shown, we have noted a time-sequence consistency between the 4 June 2011 neutron event and the EUV late-phase events of *Woods et al.* [2011]. In particular, 1–3 h after the prompt phase, acceleration effects are observed to take place higher in the corona than during the early portion of these events [*Woods et al.*, 2011]. This observation is qualitatively consistent with the statements given by *Vilmer et al.* [2011] that proton and alpha interactions with heavy ions will preferentially occur in low-density environments, such as the upper corona. In any case, the observation of the 4 June 2011 neutrons strongly suggests that a substantial number of low-energy threshold reactions were taking place. This observation can be used to place constraints on the population and energy content of heavy ions near the Sun.

[73] Aside from prompting future work to understand ion acceleration processes in light of this measurement, other implications can be drawn from the 4 June 2011 detection of neutrons. First, the strong evidence that points toward a solar origin for these neutrons demonstrates the feasibility of using MESSENGER NS data for detecting and characterizing solar neutrons. However, the large singles count rate during the neutron event is not fully understood, and more analysis and modeling work should be done to understand the mix of particle species that could produce this behavior. We note that had the MESSENGER spacecraft included instruments that could make high-energy charged-particle measurements of the type on the STEREO spacecraft, these remaining ambiguities could have been understood. Further, with the new information provided by the 4 June 2011 event, the evidence for and against the solar origin of the 31 December 2007 event [*Feldman et al.*, 2010; *Share et al.*, 2011] should be reevaluated. Absent the 4 June 2011 event, the marked difference between the expected and measurement-derived fluence magnitude of the 31 December 2007 event suggested that the neutrons from that event might not have had a solar origin. However, now that the implied fluence magnitude of the 4 June 2011 event is seen to be similar to that of the 31 December 2007 event, the large discrepancy between the expected and implied event size can no longer be used a priori to argue that the neutrons of 31 December 2007 are not of solar origin. In addition, the revised calculations of SEP-generated neutrons with appropriate low-energy cross sections (section 4.1) show that the measured neutrons are still more than a factor of 2 larger than the upper limit on the production by SEP ions.

[74] Finally, the NS data should be further studied to identify additional candidate neutron events and to determine which, if any, may have characteristics consistent with a solar origin. Other solar events have been seen at MESSENGER during the time the spacecraft has been in orbit at Mercury, but the 4 June 2011 event shows the clearest evidence for a solar origin of any detected neutron event to date. This result indicates that such events are rare. As of this writing, the MESSENGER spacecraft has sufficient propellant to continue operating through the first quarter of 2015. Further understanding of neutron events of the type documented here will require additional modeling and analysis of existing events, additional observation time with the MESSENGER NS, and ultimately new measurements made with neutron detectors that travel to within 0.3 AU and closer to the Sun.

Appendix A: NS Dead Time

[75] The MESSENGER NS was not designed for high count rate applications, as its primary design goal is to measure planetary neutrons during solar quiet times. As a consequence, quantifying the instrument dead time involves an empirically driven analysis that contains systematic uncertainties. Estimates of the NS dead time are made using several onboard sensor counters. The overall NS dead time is controlled by a maximum event processing time of 25 μs. This is the maximum time required for events to be processed by the NS front-end and field programmable gate array electronics. However, some events take less processing time than the full 25 μs. Thus, the effective dead time of the NS system will be less than 25 μs per event.

[76] The input count rate, $C_{\mathrm{NS,\,input}}$, can be estimated using the count rate from the singles hardware counter, C_{singles}, for each of the NS sensors. This total count rate must be corrected for double counting of various events, $C_{\mathrm{correction}}$:

$$C_{\mathrm{NS,\,input}} = C_{\mathrm{singles}} - C_{\mathrm{correction}}. \tag{A1}$$

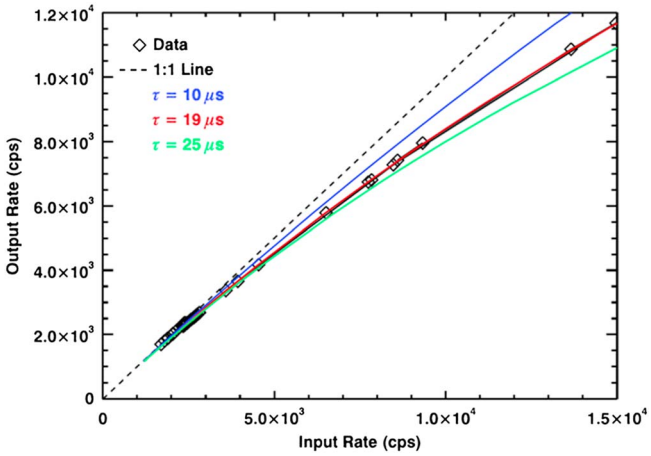

Figure A1. Input rate versus output rate as calculated with equations (A6) and (A7) (diamonds). The 1:1 correlation is shown by the dashed line. Dead-time model values from equation (A4) are shown for $\tau = 10\,\mu s$ (blue line), 19 μs (red line), and 25 μs (green line).

[77] The output count rate is given by a rate from a total software event counter, C_{SW}, so that

$$C_{NS,\,output} = C_{SW}. \tag{A2}$$

[78] The singles hardware count rates are given by

$$C_{singles} = C_{LG1} + C_{LG2} + C_{BP}, \tag{A3}$$

where C_{LG1}, C_{LG2}, and C_{BP} are the singles count rates for each of the LG1, LG2, and BP sensors, respectively. These hardware counters are themselves affected by a hardware dead time that is corrected using a nonparalyzable dead-time model [*Knoll*, 2000]:

$$C_{input} = \frac{C_{output}}{1 - C_{output}\tau}. \tag{A4}$$

where C_{input} and C_{output} are generic input and output count rates, respectively, and τ is the hardware dead time per event.

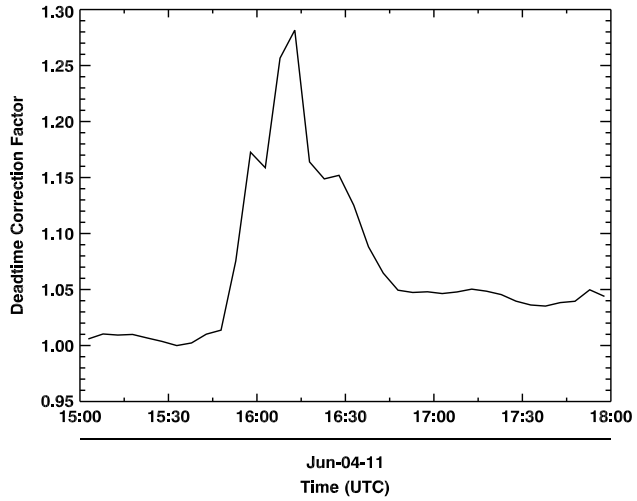

Figure A2. Calculated dead-time correction factor ($f_{DT} = C_{input}/C_{output}$) for the 3 h around the fast-neutron event on 4 June 2011.

Prior to launch, the sensor hardware dead times were determined to be $\tau_{LG1} = 7.8\,\mu s$, $\tau_{LG2} = 8.1\,\mu s$, and $\tau_{BP} = 7.8\,\mu s$. Dead-time-corrected hardware count rates C_{LG1}, C_{LG2}, and C_{BP} are obtained by applying equation (A4) to the measured count rates.

[79] There are multiple corrections that must be applied in equation (A1) through the term $C_{correction}$. First, BP reset events, at a count rate $C_{BP\ reset}$, produce double counts in the BP hardware counter, so the BP reset count rate must be subtracted from the BP input count rate. Second, double- and triple-coincidence events are single events but are counted in each of the hardware counters. The total coincident count rate,

$$C_{coin} = C_{LG1,\,DBL} + C_{LG2,\,DBL} + 2C_{triple}, \tag{A5}$$

therefore, must be subtracted from the input count rates. Here the triple-coincidence count rate is multiplied by 2 because it contributes approximately two extra counts in the total hardware counters. The coincidence counters are software rather than hardware counters, and they are subject to the software dead time per event of <25 μs. To account for this fact, the coincidence count rates are moved to the output side of the count rates with a change of sign. In summary, the input and output count rates are estimated from

$$C_{NS,\,input} = C_{LG1} + C_{LG2} + C_{BP} - C_{BP\ reset} \tag{A6}$$

and

$$C_{NS,\,output} = C_{SW} + C_{LG1,\,DBL} + C_{LG2,\,DBL} + 2C_{triple}. \tag{A7}$$

[80] The input and output count rates defined by equations (A6) and (A7) for 3 h of time around the neutron event are shown in Figure A1. The data are best fit by a system dead time of $\tau = 19\,\mu s$. As expected, this figure is lower than the maximum 25 μs dead time per event and reflects the reality that some NS events are processed more quickly than 25 μs.

[81] A dead-time correction factor, $f_{DT} = C_{NS,\,input}/C_{NS,\,output}$, can be calculated. As seen in Figure A2, this correction factor reaches a maximum of 1.25 near the center of the neutron event. All measured count rates are multiplied by this correction factor

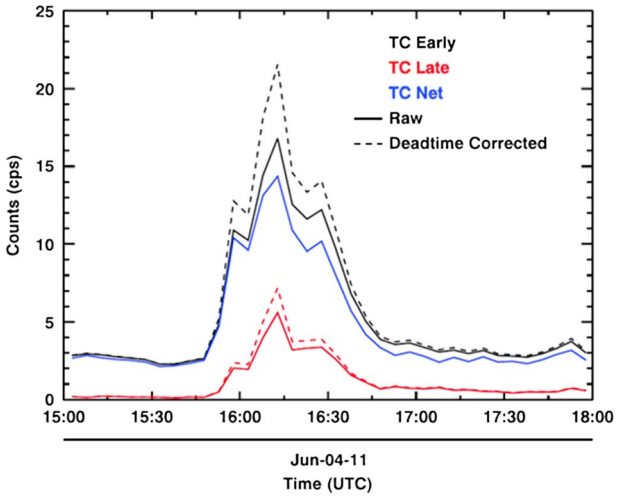

Figure A3. Raw (black/red solid line) and dead-time-corrected (black/red dashed line) time-correlated (TC) fast-neutron counts. Final net fast-neutron counts are shown as the TC net (blue line) count rate.

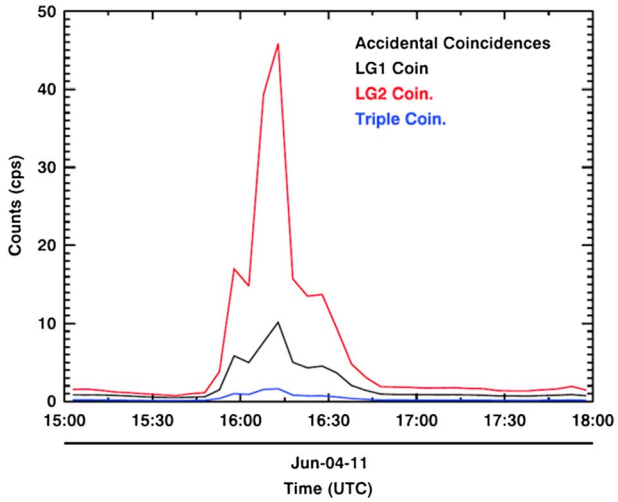

Figure A4. Accidental coincidence for the three NS coincidence counters calculated with equation (A8).

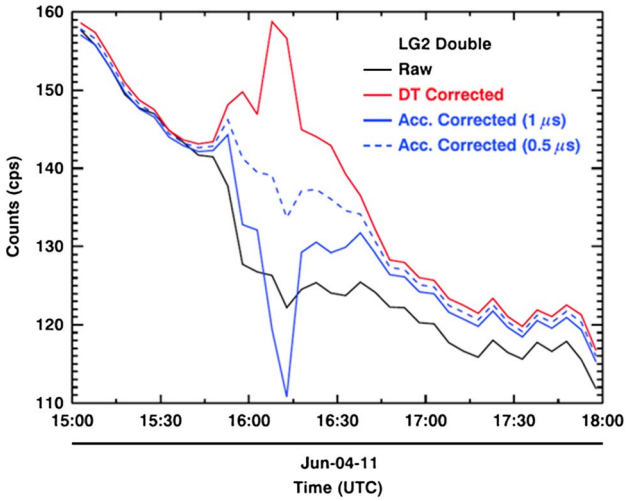

Figure A6. LG2-BP double-coincidence count rates for raw uncorrected (black line), dead-time corrected (red line), and accidental corrected with a 1 μs coincidence window (blue line). Accidental corrected with a 0.5 μs window is shown as a blue dashed line.

to arrive at dead-time-corrected count rates. An example is given in Figure A3, which shows the BP time-correlated (TC) fast-neutron count rates both before and after the dead-time corrections. The final fast-neutron count rate (blue line in Figure A3) is determined with dead-time-corrected TC count rates and reflects the net fast neutrons after accounting for accidental counts as measured by the BP TC late counter.

[82] The coincidence counters require an additional correction to account for accidental coincidences. The approximate width of the coincidence window for the coincidence counters is $\tau_{acc} = 1$ μs. The accidental count rates are then

$$\begin{aligned} C_{\mathrm{LG1,\ acc.}} &= C_{\mathrm{LG1}} C_{\mathrm{BP}} \tau_{\mathrm{acc}} \\ C_{\mathrm{LG2,\ acc.}} &= C_{\mathrm{LG2}} C_{\mathrm{BP}} \tau_{\mathrm{acc}} \\ C_{\mathrm{triple,\ acc.}} &= \left(C_{\mathrm{LG1,\ DBL}} C_{\mathrm{LG2}} + C_{\mathrm{LG2,\ DBL}} C_{\mathrm{LG1}}\right) \tau_{\mathrm{acc}}. \end{aligned} \tag{A8}$$

[83] Figure A4 shows the accidental coincidence count rates for each sensor. The LG2 accidental count rate is the largest of the three because it also has the largest singles count rate (see Figure 6). These accidental count rates are subtracted from the dead-time-corrected coincidence count rates to arrive at a final coincidence count rate measurements.

[84] Time series for each coincidence count rate counter are shown in Figures A5, A6 and A7. As seen, for all coincidence count rates, there is a relative decrease at the same time as the maximum fast-neutron count rate. Whereas such an observed decrease may represent a true decrease in the flux of GCR-generated charged particles, it is not clear what physical mechanism could drive such a decrease in charged-particle flux. On the other hand, it is possible that the observed

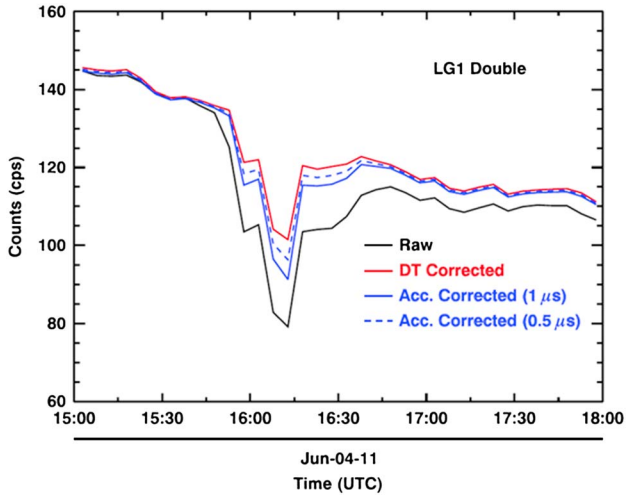

Figure A5. LG1-BP double-coincidence count rates for raw uncorrected (black line), dead-time corrected (red line), and accidental corrected with a 1 μs coincidence window (blue line). Accidental corrected with a 0.5 μs window is shown as a blue dashed line.

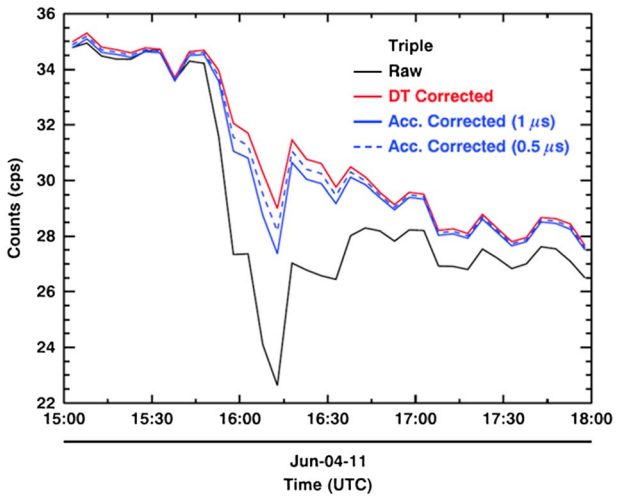

Figure A7. LG1-BP-LG2 triple-coincidence count rates for raw uncorrected (black line), dead-time corrected (red line), and accidental corrected with a 1 μs coincidence window (blue line). Accidental corrected with a 0.5 μs window is shown as a blue dashed line.

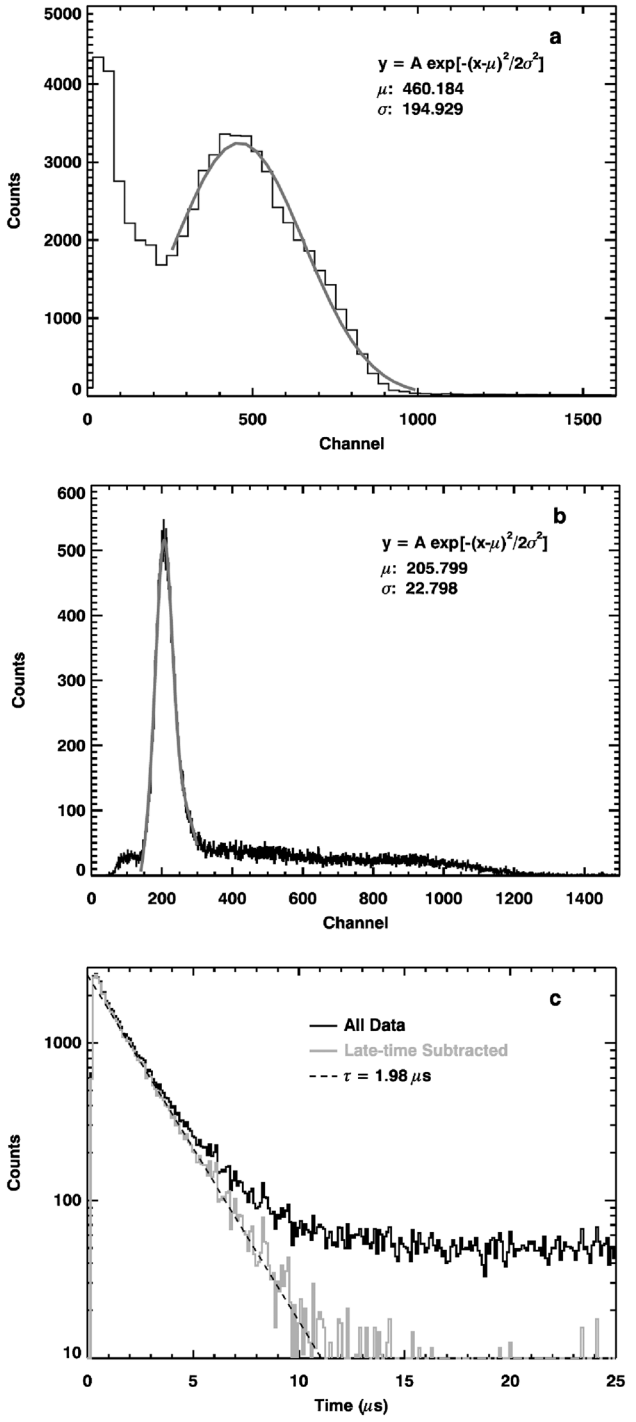

Figure B1. NS event mode histograms from preflight calibration data for an incident neutron energy of 1.5 MeV. (a) Prompt-pulse histogram data along with a Gaussian fit to the main peak. Peak position and width parameters are shown. (b) Delayed pulse histogram data along with a Gaussian fit to the main peak. Peak position and width parameters are shown. (c) Full TTSP histogram data along with a late-time-subtracted histogram and an exponential fit to the late-time-subtracted histogram.

decrease may rather be the result of imperfect dead-time and accidental coincidence corrections. For example, if a coincidence window of 0.5 μs instead of 1 μs is used for the accidental coincidence correction, the LG2 decrease almost disappears (dashed trace in Figure A6). In a similar manner, other empirical constants might not yet be determined with sufficient accuracy to eliminate all systematic errors in the dead-time and accidental coincidence corrections. In principle, better estimates of these constants can be determined from new measurements with the ground-based NS engineering model. However, such improvements will not change the overall conclusions of this study, namely, that a large count rate of fast neutrons was detected on 4 June 2011 at 15:45 UTC and that this fast-neutron event was not accompanied by a correspondingly large flux of charged particles. This conclusion is supported not only by the measured coincidence count rates (even within the systematic uncertainties described in this section) but also by the gamma-ray data described in section 4.

Appendix B: Calibration of NS Fast-Neutron Energy Scale and Energy Spreading

[85] Here we describe the fast-neutron channel-to-energy calibration that was carried out with the NS prior to launch. In March 2004, the flight NS sensor and electronics were taken to the Columbia University Radiological Research Accelerator Facility, where it was exposed to monoenergetic neutrons having energies from 0.5 to 14 MeV. The NS was placed inside a small beam room such that the surrounding concrete walls were located approximately 150–200 cm from the NS. Pulse-height histograms of NS event mode data taken with a neutron beam energy of 1.5 MeV are shown in Figure B1. The prompt pulse (Figure B1a), which is a measure of the neutron energy into the BP sensor, shows a clear peak around channel 460. The delayed and TTSP histograms are shown in Figures B1b and B1c, with measured distribution parameters shown on the figures.

[86] To derive the neutron energy scale, the peak position of the prompt pulse was measured for all energies ranging from 0.5 to 14 MeV. Figure B2 shows that the peak positions are well fit by a power law relation

$$E = ax^b, \tag{B1}$$

where E is the incident neutron energy, x is the channel position, and the fitted power law parameters are $a = 0.039$ and $b = 0.601$. The power law exponent of 0.601 compares

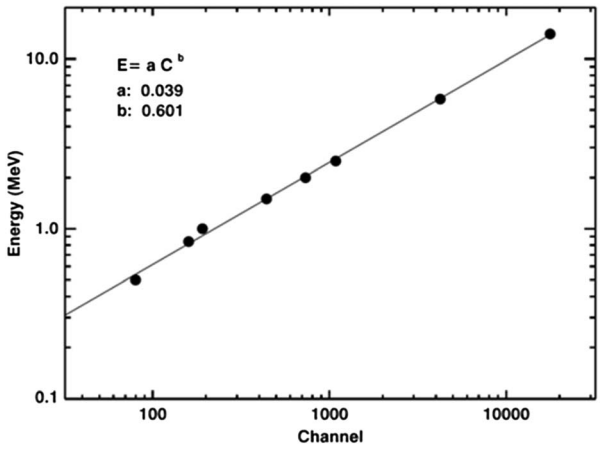

Figure B2. Incident neutron energy versus peak position of the prompt pulse. Power law fit parameters are shown.

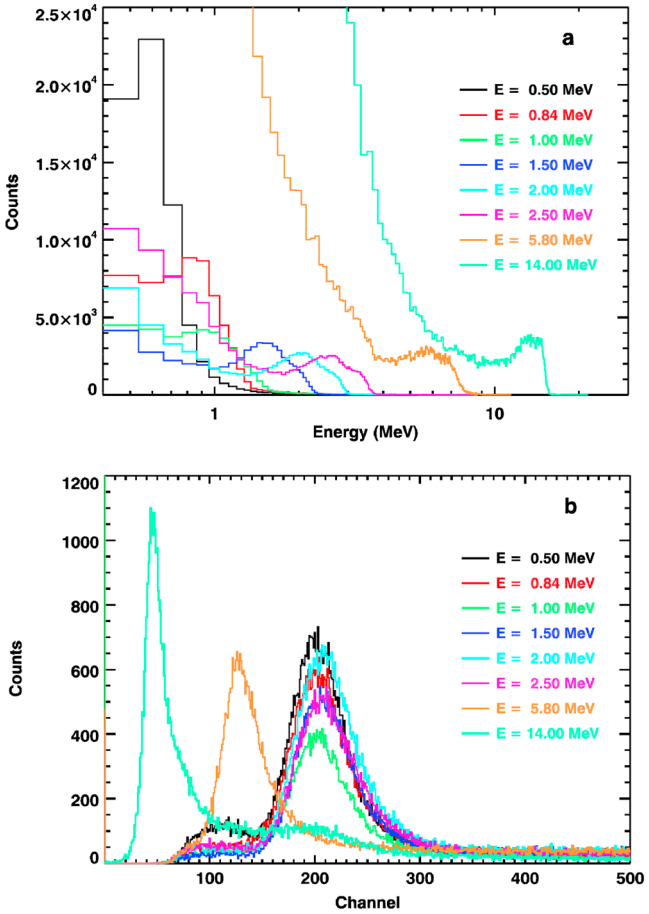

Figure B3. (a) Prompt-pulse histograms versus calibration neutron energy for all incident neutron energies from 0.5 to 14 MeV. (b) Delayed pulse histograms versus channel number for all incident neutron energies from 0.5 to 14 MeV.

favorably with the value 0.625 determined by *Byrd and Urban* [1994] for a similar borated plastic scintillator.

[87] The prompt and delayed histograms for all incident neutron energies are shown in Figure B3, scaled in energy.

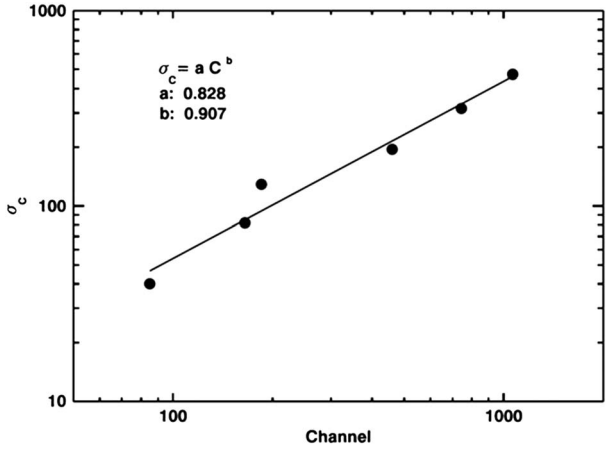

Figure B4. Energy resolution in channel space, σ_c, as a function of channel for calibration data with input energies ranging from 0.5 to 2.5 MeV.

For the highest energies ($E > 5$ MeV), there is substantial room background from scattered neutrons, and the full-energy peaks diverge from the nearly Gaussian shape seen for lower energies (Figure B1a). As a consequence, there are uncertainties in determining precisely the peak channel position for these highest-energy peaks. If alternative peak positions still consistent with observations are selected, the energy scale derived with equation (B1) can change by up to 25%. In sections 5.3 and 5.4, we apply such a scale change in order to match the forward model energy spectra and data. On the basis of our understanding of the channel-to-energy calibration, application of such a scale factor is consistent with the uncertainties in the calibration. We finally note that for the two highest energies (5.8 and 14 MeV), the NS high-voltage gain was lowered to enable the pulse heights to stay on scale within the NS electronics. This gain shift, which was taken into account in the energy calibration, is seen in Figure B3b.

[88] For flight data, the NS gain characteristics will not necessarily be the same as for the preflight calibration. The peak position of the delayed pulse can therefore be used as an anchor for any NS gain configuration under the assumption that the power law exponent remains constant. From Figure B1b, the peak position of the delayed pulse during the preflight calibration was $x_{D,0} = 206$. From equation (B1), this figure translates to an equivalent neutron energy of $E_{D,0} = 0.958$ MeV. Since this energy deposition is constant for any gain configuration, a general multiplicative constant, a', can be expressed as

$$a' = 0.958/x_D^b, \tag{B2}$$

where x_D is the peak position of the delayed peak for any NS gain setting and b is the same exponent as before.

[89] To carry out the energy spectrum forward modeling, the intrinsic energy spreading of the NS needs to be known. For the lower-energy calibration data ($E \leq 2.5$ MeV), the room background is sufficiently small and the neutron full energy is sufficiently separated to enable the Gaussian width of the prompt peaks to be measured (see Figure B1). The width for input energies from 0.5 to 2.5 MeV was measured

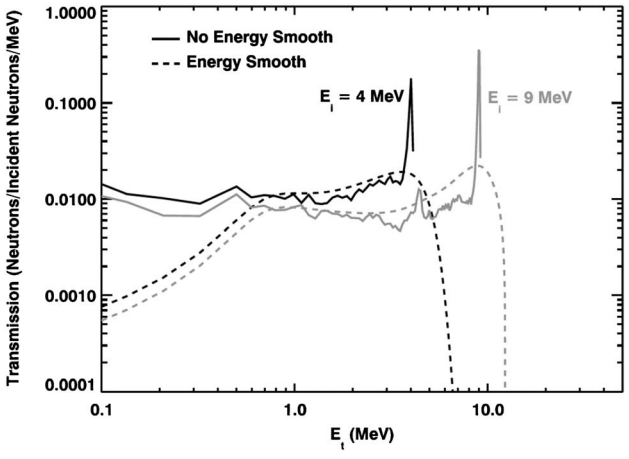

Figure C1. Transmission function $C(E_t) = F(E_t)\Delta E_t$ for spacecraft-incident energies of 4 MeV (black line) and 9 MeV (gray line). The solid lines show the function prior to energy spreading and the dashed lines show the function after energy spreading.

and is shown in Figure B4. The energy resolution ranges from 40% at higher energies to 50% at lower energies and is well fit by a power law function

$$\sigma_x = 0.828x^{0.907}. \quad \text{(B3)}$$

Appendix C: Spacecraft Transmission Function, $T(E,E_t)$

[90] The spacecraft transmission function, $T(E,E_t)$, is calculated with the particle transport code MCNPX [*Pelowitz*, 2005]. The calculation uses a full material model of the MESSENGER spacecraft that has been validated for prior measurements of planetary neutrons [*Lawrence et al.*, 2010, 2013] and specifically uses the Mercury orbital configuration with the spacecraft fuel tanks mostly empty. For the forward model described in section 5, the transmission function is calculated with 95 incident energies on the sunshade side of the spacecraft ranging from 0.5 to 9.9 MeV in steps of 0.1 MeV. The MCNPX transport model does not account for the energy spreading in the NS, so this energy spreading is applied separately as described below. As described in Appendix B, the energy spreading was measured in channel space as a power law function (equation (B3)). Therefore, the neutron transmission must be transformed into channel space prior to applying the energy spreading.

[91] Let E_i be a given incident energy on the spacecraft. We then define

$$F(E_t) \equiv T(E_i, E_t). \quad \text{(C1)}$$

[92] MCNPX returns the total neutrons per incident neutron, C, within an energy bin ΔE_t so that $C(E_t) = F(E_t)\,\Delta E_t$. To transform into channel space, we note that the integrals of $F(E_t)dE_t$ and $F(x)dx$ have to be equal because they are measuring the same distribution. Therefore,

$$F(E_t)dE_t = F(x)dx, \quad \text{(C2)}$$

so that

$$F(x) = F(E_t)\frac{dE_t}{dx}. \quad \text{(C3)}$$

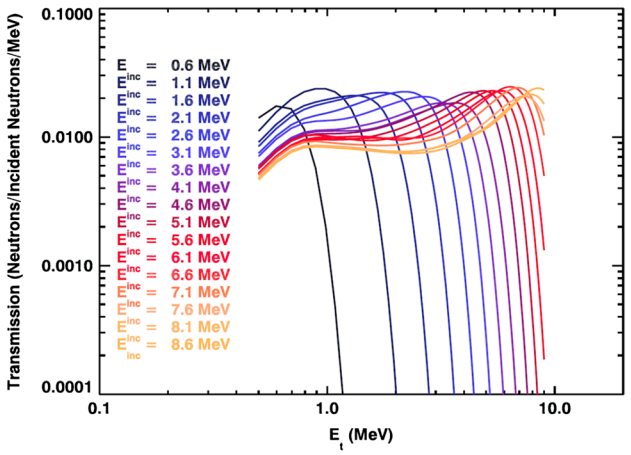

Figure C2. Transmission function $C_s(E_t)$ with energy spreading for a range of spacecraft-incident energies from 0.6 to 8.6 MeV; different incident energies are shown by different colors.

[93] The binned channel flux, $C(x)$, is then calculated from the MCNPX binned energy flux, $C(E_t)$ by

$$C(x) = \frac{C(E_t)}{\Delta E_t}\frac{dE_t}{dx}. \quad \text{(C4)}$$

[94] Prior to the energy spreading, a threshold of 0.5 MeV is applied to the initial energy flux such that $C(E_t) = 0$ for all $E_t < 0.5$ MeV. This threshold is applied to mimic the operation of the NS, for which energies less than ~0.5 MeV do not give a measurable double-pulse fast-neutron interaction. From equation (B3), the binned channel flux is smoothed to create $C_s(x)$ using a running averaged smoothing algorithm with a channel-dependent and normalized Gaussian kernel. The smoothed, channel-space-binned flux is converted back into energy space with the inverse transformation

$$C_s(E_t) = C_s(x)\frac{dx}{dE_t}\Delta E_t. \quad \text{(C5)}$$

and the final transmission function used in equation (5) is $T(E_i, E_t) = C_s(E_t)/\Delta E_t$. Figure C1 shows the energy-binned functions $C(E_t)$ and $C_s(E_t)$ for incident energies of $E_i = 4$ MeV and $E_i = 9$ MeV. Figure C2 shows $C_s(E_t)$ for a range of incident energies onto the front of the spacecraft.

[95] **Acknowledgments.** The authors are grateful to the entire MESSENGER team for their invaluable and skillful contributions to the development and operation of the MESSENGER spacecraft. We thank the Caltech STEREO Science Data Center for making STEREO energetic particle data available. The authors also thank Richard Mewaldt for helpful discussions regarding STEREO energetic particle data. This paper was substantially improved by the diligent work of an anonymous reviewer. The MESSENGER project is supported by the NASA Discovery Program under contract NAS5-97271 to The Johns Hopkins University Applied Physics Laboratory (JHU/APL) and NASW-00002 to the Carnegie Institution of Washington. Substantial support for the analysis work was provided by the NASA Solar and Heliophysics Program under grant NNX12AB33G to JHU/APL. All original data reported in this paper are archived by the NASA Planetary Data System.

[96] Philippa Browning thanks the reviewers for their assistance in evaluating this paper.

References

Brown, V. R., C. Wong, C. H. Poppe, J. D. Anderson, J. C. Davis, S. M. Grimes, and V. A. Madsen (1986), Cross sections for the Ti(p,n) reaction to analogs of ground and 2+ excited states, *Phys. Rev. C*, *33*, 1235–1246.

Byrd, R. C., and W. T. Urban (1994), *Calculations of the Neutron Response of Boron-Loaded Scintillators*, Report LA-12833-MS, Los Alamos Natl. Lab, Los Alamos, N. M.

Desai, M. I., R. G. Marsden, T. R. Sanderson, D. Lario, E. C. Roelof, G. M. Simnett, J. T. Gosling, A. Balogh, and R. J. Forsyth (1999), Energy spectra of 50-keV to 20 MeV protons accelerated at corotating interactions regions at Ulysses, *J. Geophys. Res.*, *107*, 6705–6719, doi:10.1029/1998JA900176.

Dorman, L. I. (2010), *Solar Neutrons and Related Phenomena*, 873 pp., Springer, New York.

Ellison, D. C., and R. Ramaty (1985), Shock acceleration of electrons and ions in solar flares, *Astrophys. J.*, *298*, 400–408.

Evans, L. G., et al. (2012), Major-element abundances on the surface of Mercury: Results from the MESSENGER Gamma-Ray Spectrometer, *J. Geophys. Res.*, *117*, E00L07, doi:10.1029/2012JE004178.

Feldman, W. C., et al. (1989), The Solar Probe mission, in *Particle Astrophysics*, *Conf. Proc. Ser.*, vol. 203, pp. 101–110, American Institute of Physics, Melville, N. Y.

Feldman, W. C., et al. (2002), Fast neutron flux spectrum aboard Mars Odyssey during cruise, *J. Geophys. Res.*, *107*(A6), 1083, doi:10.1029/2001JA000295.

Feldman, W. C., et al. (2010), Evidence for extended acceleration of solar-flare ions from 1–8 MeV solar neutrons detected with the MESSENGER

Neutron Spectrometer, *J. Geophys. Res.*, *115*, A01102, doi:10.1029/2009JA014535.

Goldsten, J. O., et al. (2007), The MESSENGER Gamma-Ray and Neutron Spectrometer, *Space Sci. Rev.*, *131*, 339–391.

Hua, X.-M., B. Kozlovsky, R. E. Lingenfelter, R. Ramaty, and A. Stupp (2002), Angular and energy-dependent neutron emission for solar flare magnetic loops, *Astrophys. J. Suppl. Ser.*, *140*, 563–579.

Kim, K. J., D. M. Drake, R. C. Reedy, R. M. S. Williams, and W. V. Boynton (2007), Theoretical fluxes of gamma rays from the Martian surface, *J. Geophys. Res.*, *112*, E03S09, doi:10.1029/2005JE002655.

Knoll, G. F. (2000), *Radiation Detection and Measurement*, 3rd ed., 802 pp., Wiley, New York.

Koning, A. J., and D. Rochman (2012), Modern nuclear data evaluation with the TALYS code system, *Nucl. Data Sheets*, *113*, 2841–2934, doi:10.1016/j.nds.2012.11.002.

Lario, D., M.-B. Kallenrode, R. B. Decker, E. C. Roelof, S. M. Krimigis, A. Aran, and B. Sanahuja (2006), Radial and longitudinal dependence of solar 4–13 MeV and 27–37 MeV proton peak intensities and fluences: HELIOS and IMP8 observations, *Astrophys. J.*, *653*, 1531–1544.

Lario, D., G. C. Ho, E. C. Roelof, B. J. Anderson, and H. Korth (2013), Intense solar near-relativistic electron events at 0.3 AU, *J. Geophys. Res. Space Physics*, *118*, 63–73, doi:10.1002/jgra.50106.

Lawrence, D. J., W. C. Feldman, R. C. Elphic, J. J. Hagerty, S. Maurice, G. W. McKinney, and T. H. Prettyman (2006), Improved modeling of Lunar Prospector Neutron Spectrometer data: Implications for hydrogen deposits at the lunar poles, *J. Geophys. Res.*, *111*, E08001, doi:10.1029/2005JE002637.

Lawrence, D. J., W. C. Feldman, J. O. Goldsten, T. J. McCoy, D. T. Blewett, W. V. Boynton, L. G. Evans, L. R. Nittler, E. A. Rhodes, and S. C. Solomon (2010), Identification and measurement of neutron-absorbing elements on Mercury's surface, *Icarus*, *209*, 195–209.

Lawrence, D. J., et al. (2013), Evidence for water ice near Mercury's north pole from MESSENGER Neutron Spectrometer measurements, *Science*, *339*, 292–296, doi:10.1126/science.1229953.

Lawrence, D. J., W. C. Feldman, R. E. Gold, J. O. Goldsten, and R. L. McNutt (2014), The Neutron, Gamma-ray, X-ray Spectrometer (NGXS): A compact instrument for making combined measurements of neutrons, gamma-rays, and X-rays, *Acta Astronaut.*, *93*, 524–529, doi:10.1016/j.actaastro.2012.06.017.

Lesko, K. T., E. B. Norman, R. M. Larimer, S. Kuhn, D. M. Meekhof, S. G. Crane, and H. G. Bussell (1988), Measurements of cross sections relevant to γ-ray line astronomy, *Phys. Rev. C*, *37*(5), 1808–1817.

Maurice, S., W. C. Feldman, D. J. Lawrence, O. Gasnault, C. d'Uston, and P. G. Lucey (2000), High-energy neutrons from the Moon, *J. Geophys. Res.*, *105*, 20,365–20,375, doi:10.1029/1999JE001151.

McKinney, G. W., D. J. Lawrence, T. H. Prettyman, R. C. Elphic, W. C. Feldman, and J. J. Hagerty (2006), MCNPX benchmark for cosmic ray interactions with the Moon, *J. Geophys. Res.*, *111*, E06004, doi:10.1029/2005JE002551.

Mewaldt, R. A. (2006), Solar energetic particle composition, energy spectra, and space weather, *Space Sci. Rev.*, *124*, 303–316, doi:10.1007/s11214-006-9091-0.

Michel, R., G. Brinkmann, H. Weigel, and W. Herr (1978), Proton-induced reactions on titanium with energies between 13 and 45 MeV, *J. Inorg. Nucl. Chem.*, *40*, 1845–1831.

Murphy, R. J., B. Kozlovsky, G. H. Share, X.-M. Hua, and R. E. Lingenfelter (2007), Using gamma-ray and neutron emission to determine solar flare accelerated particle spectra and composition and the conditions within the flare magnetic loop, *Astrophys. J. Suppl. Ser.*, *168*, 167–194, doi:10.1086/509637.

Murphy, R. J., B. Kozlovsky, and G. H. Share (2012), The production of low-energy neutrons in solar flares and the importance of their detection in the inner heliosphere, *Astrophys. J. Suppl. Ser.*, *202*, 1–32, doi:10.1088/0067-0049/202/1/3.

Nieto, M. M., W. C. Feldman, and D. J. Lawrence (2008), Testing the unitarity of the CKM matrix with a space-based neutron decay experiment, *Mod. Phys. Lett. A*, *23*, 1735–1743, doi:10.1142/S0217732308027187.

Nittler, L. R., et al. (2011), The major element composition of Mercury's surface from MESSENGER X-ray spectrometry, *Science*, *333*, 1847–1850.

Pelowitz, D. B. (Ed.) (2005), *MCNPX User's Manual Version 2.5.0*, Report LA-CP-05-0369, Los Alamos Natl. Lab., Los Alamos, N. M.

Peplowski, P. N., et al. (2011), Radioactive elements on Mercury's surface from MESSENGER: Implications for the planet's formation and evolution, *Science*, *333*, 1850–1852, doi:10.1126/science.1211576.

Peplowski, P. N., et al. (2012), Variations in the abundances of potassium and thorium on the surface of Mercury: Results from the MESSENGER Gamma-Ray Spectrometer, *J. Geophys. Res.*, *117*, E00L04, doi:10.1029/2012JE004141.

Prettyman, T. H., et al. (2004), Composition and structure of the Martian surface at high southern latitudes from neutron spectroscopy, *J. Geophys. Res.*, *109*, E05001, doi:10.1029/2003JE002139.

Prettyman, T. H., et al. (2011), Dawn's gamma ray and neutron detector, *Space Sci. Rev.*, *163*, 371–459, doi:10.1007/s11214-011-9862-0.

Reames, D. V., and C. K. Ng (2010), Streaming-limited intensities of solar energetic particles on the intensity plateau, *Astrophys. J.*, *723*, 1286–1293, doi:10.1088/0004-637X/723/2/1286.

Reedy, R. C. (1978), Planetary gamma-ray spectroscopy, Proc. Lunar Planet. Sci. Conf., 9th, 2961–2984.

Ryan, J. M. (2000), Long-duration solar gamma-ray flares, *Space Sci. Rev.*, *93*, 581–610, doi:10.1023/A:1026547513730.

Schlemm, C. E., II, et al. (2007), The X-Ray Spectrometer on the MESSENGER spacecraft, *Space Sci. Rev.*, *131*, 393–415, doi:10.1007/s11214-007-9248-5.

Share, G. H., R. J. Murphy, A. J. Tylka, B. Kozlovsky, J. M. Ryan, and C. Gwon (2011), Physics of solar neutron production: Questionable detection of neutrons from the 31 December 2007 flare, *J. Geophys. Res.*, *116*, A03102, doi:10.1029/2010JA015930.

Vilmer, N., M. Maksimovic, R. P. Lin, and G. Trottet (2001), Ion acceleration in solar flares: Low energy neutron measurements, in *Solar Encounter: Proceedings of the First Solar Orbiter Workshop, Puerto de la Cruz, Tenerife, Spain, May 14–18*, *Spec. Publ.*, vol. 493, edited by B. Battrick and H. Sawaya-Lacoste, pp. 405–410, European Space Agency, Noordwijk, Netherlands.

Vilmer, N., A. L. MacKinnon, and G. J. Hurford (2011), Properties of energetic ions in the solar atmosphere from γ-ray and neutron observations, *Space Sci. Rev.*, *159*, 167–224, doi:10.1007/s11214-010-9728-x.

Woods, T. N., et al. (2011), New solar extreme-ultraviolet irradiance observations during flares, *Astrophys. J.*, *739*, 59, doi:10.1088/0004-637X/739/2/59.

Woolf, R. S., J. M. Ryan, P. F. Bloser, U. Bravar, E. O. Flückiger, J. S. Legere, A. MacKinnon, P. C. Mallik, M. L. McConnell, and B. Pirard (2009), Advanced characterization and simulation of SONNE: A fast neutron spectrometer for Solar Probe Plus, *Proc. SPIE*, *7438*, 74380S, doi:10.1117/12.826425.